Effects of cavitation on the hydrodynamic loading and wake vortex evolution of a pre-swirl pump-jet propulsor

Ocean Engineering 266 (2022) 113069

Contents lists available at ScienceDirect

Ocean Engineering

journal homepage: www.elsevier.com/locate/oceaneng

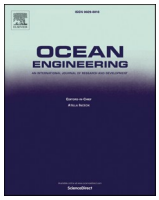

Effects of cavitation on the hydrodynamic loading and wake vortex evolution of a pre-swirl pump-jet propulsor

Xutao Zhao [a], Xi Shen [a], Linlin Geng [a], Desheng Zhang [a,*], B.P.M. (Bart) van Esch [b]

[a] Research Center of Fluid Machinery Engineering and Technology, Jiangsu University, Zhenjiang, 212013, China
[b] Department of Mechanical Engineering, Eindhoven University of Technology, Eindhoven, 5600MB, the Netherlands

ARTICLE INFO

Keywords:
Pump-jet propulsor
Cavitation
Vortex structures
Cavitation-vortex interaction

ABSTRACT

The purpose of this study is to investigate the effects of cavitation on the hydrodynamic loading and wake vortex evolution in a pre-swirl pump-jet propulsor, and also the cavitation-vortex interaction mechanism. The cavitating flow is simulated by delayed detached eddy simulation coupled with a homogeneous cavitation model. Based on available experimental validation, the cavitation patterns, hydrodynamic loadings, the tip leakage vortex (TLV) evolutions and trailing edge vortex interactions are orderly investigated under two typical cavitation conditions. Results show that the blade sheet cavitation, TLV cavitation and tip clearance cavitation are regard as the main cavitation types of the rotor, where the sheet cavity on adjacent blades is non-uniformly distributed under the perturbations of the stator wakes and phase effects. The interaction between the thickening sheet cavity and stator wakes causes the shift of dominant frequencies of rotor loading from the rotor blade passing frequency f_{BPF} and its harmonics to stator blade passing frequency f_S and its harmonics. The relative vorticity transport equation is used to analyze cavitation-vortex interaction of TLV. The TLV cavitation promotes the vorticity production of TLV at the incipient stage and increases its intensity downstream. The instability of TLV is triggered earlier when cavitation is heavy due to the enhanced mutual interaction between consecutive spirals of the TLVs and their interaction with sheet cavity induced shedding vortices. The trailing edge vortices of stator and rotor mutually interacts with blade sheet cavity, which accelerates the breakdown of trailing vortex system downstream.

1. Introduction

The pump-jet propulsor (PJP) is a new alternative propulsion equipment developed in recent years, which mainly used for underwater vehicles. Compared to conventional propellers, the PJP offers superior performance with high propulsion efficiency and low radiated noise during actual cruising (McCormick and ElSenhuth, 1963; Shirazi et al., 2019; Suryanarayana et al., 2010a; Jiao et al., 2022). The PJP with a pre-swirl stator in front of the axial flow rotor is the so-called pre-swirl stator PJP which is specially designed for submarines (Qin et al., 2021a). Cavitation occurrence is inevitable in this kind of PJP when it operates in complex marine environments with high speed, which leads to undesirable propulsion performance degradation (Suryanarayana et al., 2010b). In addition, due to the disturbed oncoming flow with spatial non-uniformity and temporal unsteadiness, the cavitation-vortex interaction always happens around rotating rotor which deteriorates the vibration and noise performance of propulsion system as well. Investigating the cavitation patterns, vortical structures and their interactions in the pre-swirl stator PJP is crucial for the optimization design of vehicle propulsion system.

The cavitation characteristics of axial flow pumps has been studied for many years. Rains (1954) firstly observed the tip cavitation in an axial flow pump, some special attentions were paid to its formation, migration, and collapse by employing high-speed visualizations. Laborde (Laborde et al., 1997) investigated the inception of tip clearance cavitation and tip leakage vortex (TLV) cavitation in various axial flow pumps with different tip clearance sizes and blade geometries. Tan et al. (David Y. Tan et al., 2012a) experimentally studied the cavitation structures in an axial waterjet pump under varying flow and pressure conditions, some interesting cavitation phenomena including the sheet cavitation on the blade suction surface (SS), alternate blade cavitation, large-scale cavity instabilities, the TLV cavitation and its interactions with sheet cavitation were highlighted in a systematic way. Based on some beneficial findings, Tan et al. (2015) and Chen et al. (2020) further elucidated the underlying mechanisms for cavitation caused performance breakdown of the waterjet pump. In addition, some special

* Corresponding author.
E-mail address: zds@ujs.edu.cn (D. Zhang).

https://doi.org/10.1016/j.oceaneng.2022.113069
Received 14 September 2022; Received in revised form 13 October 2022; Accepted 28 October 2022
Available online 13 November 2022

perpendicular cavitating vortices (PCVs) induced by the interaction of TLV cavitation and sheet cavitation on the blade SS were observed and analyzed. Zhang et al. (Shen et al., 2021; Zhang et al., 2015a, 2015b) carried out a series of cavitating flow numerical simulations of axial flow pumps based on the available experimental validation. The cavitation dynamics around the rotor tip region were thoroughly investigated through iso-surfaces of cavities, vorticity fields and velocity vector fields. The temporal and spatial evolutions of PCVs were well captured by improved numerical method. The cavitation patterns in hydraulic propulsion systems disturbed by the non-uniform oncoming flow have also been discussed by numerous scholars (Ge et al., 2020; Ji et al., 2012a, 2012b; Yilmaz et al., 2020). Huang (Huang et al., 2021) numerically studied the instantaneous cavitation dynamical behaviors in a mixed waterjet pump with non-uniform suction inflow. The transient cavitating flow analysis reveals that the cavities generate non-uniformly on rotating impeller blades and are varied periodically with the dominant frequency of the impeller rotating frequency. Zhao et al., 2021a, 2021b conducted experiments and numerical simulations to investigate the dynamic behaviors of blade cavitation under the perturbations of inlet guide vane (IGV) wakes for axial waterjet pump. The results show that the cavities develop non-synchronously on the adjacent blades with a phase difference. The variations of blade incidence angles due to non-uniform flow was found dominants this distinctive cavitation behavior in waterjet pump with IGVs.

For the propulsors of underwater vehicles such as propellers, duct propellers and PJPs, there are complicated vortex systems behind them with different interaction mechanisms (Gong et al., 2021; Sun et al., 2022; Wang et al., 2021a, b). The effects of cavitation on the unstable evolution of vortex systems and the interactions between them are still not clearly elucidated until now. Felli et al. (2011) experimentally investigated the evolution mechanisms of propeller wake vortices through velocity measurements and high-speed visualizations. The influence mechanisms of the spiral-to-spiral distance and the number of propeller blades on the destabilization and evolution of the tip and hub vortices were specifically highlighted. Kumar et al. (Kumar and Mahesh, 2017) carried out well-resolved large eddy simulations (LES) to analyze the instabilities of the propeller wake vortices. The interaction between the blade trailing edge vortices and the tip vortex of the adjacent blade is observed as the preferred mechanism for the wake instabilities of the objective propeller model. Gong et al. (2018) conducted a comparative numerical analysis on the evolution of wake vortices generated by ducted and non-ducted propellers in open water. The numerical results show that the interaction between the duct and the propeller directly changed the morphology of tip vortices and wake contraction. Li et al. (2021) numerically studied the evolution of the vortices in a pre-swirl stator PJP using detached eddy simulation (DES). The results show that there is a complex vortical system in the PJP. The TLV interacts with duct shed vortices and finally promotes the generation of secondary vortices. The stator wake vortices are involved in significant interactions with the rotor blade wake vortices and hub vortices. Qin et al. (Qin et al., 2021a; Qin et al., 2022a; Qin et al., 2021b) analyzed the vortex evolution in two different types of PJPs based on the DES model, and the effects of duct and the number of rotor and stator blades on the wake vortex dynamics were systematically discussed. The DES was confirmed as an efficient numerical simulation method to resolve the detailed vortical structures in propulsion systems with an acceptable computational burden.

Cavitation-vortex interaction is a complex physical process with transient evolutions which is mostly studied in some simple geometries, such as hydrofoils. Various experimental test of cavitating flow reveals that the flow instabilities and turbulence often result in the formation of large-scale vortical structures (Gopalan and Katz, 2000; Huang et al., 2013; Wang et al., 2001). Ji et al. (2014) numerically investigated the cavitation-vortex interaction around a twisted hydrofoil. The results show that cavitation promotes vortex production behind hydrofoil and increases the boundary layer thickness with local flow separation and unsteadiness. Huang et al. (2014) conducted LES to understand the interaction between unsteady cavitating flow and vortex dynamics on a 3D Clark-Y hydrofoil with the help of vorticity transport equation. Chen et al. (2021) studied the physical interaction of the cavitation-vortex dynamics around a 3D Delft hydrofoil. The different vortex identification methods are applied to identify and analyze the vortex structures. Cheng et al. (2020) carried out numerical simulations of a tip leakage cavitating flow, and the cavitation effects on vorticity and turbulence were discussed in detail. In rotating pump field, Huang et al. (2015) investigated the cavitation-vortex interaction mechanism in a mixed-flow waterjet pump. The analysis of relative vorticity transport equation indicates that the vortex stretching term contributes largely to large-scale vortex generation. Han et al. (2020) simulated tip clearance cavitating flow in a propelling pump and the tip cavitation-vortex interaction was highly focused.

For the pre-swirl stator PJP, it contains a complex vortex system with strong interaction (Li et al., 2021; Qin et al., 2021b, 2022a). If cavitation occurs to a certain extent, the interaction between cavitation and vortices will be greatly enhanced, which further affects the stability of vortex development and the exciting force level. However, most research on PJP focused on the hydrodynamic characteristics in non-cavitation conditions. It is worthwhile to study the effects of cavitation on the hydrodynamic loading and the vortex system evolution of the PJP. In this paper, the cavitating flow of pre-swirl stator PJP is simulated based on the DES method coupled with Zwart cavitation model with experimental validation. The cavitation patterns, hydrodynamic loadings, the effects of cavitation on TLV evolutions and trailing vortex interactions are orderly discussed under two typical cavitation conditions. The relative vortex transport equation is also used to elucidate the potential mechanism of cavitation-vortex interaction.

2. Numerical methodology

2.1. Governing equations

The cavitation two-phase flow is modelling based on homogenous model, the mass and momentum conservation equations are shown as follows:

$$\frac{\partial \rho_m}{\partial t}+\frac{\partial\left(\rho_m u_j\right)}{\partial x_j}=0 \tag{1}$$

$$\frac{\partial(\rho_m u_i)}{\partial t}+\frac{\partial\left(\rho_m u_i u_j\right)}{\partial x_j}=-\frac{\partial p}{\partial x_i}+\frac{\partial}{\partial x_j}\left[\mu_m+\mu_t\left(\frac{\partial u_i}{\partial x_j}+\frac{\partial u_j}{\partial x_i}-\frac{2}{3}\frac{\partial u_k}{\partial x_k}\delta_{ij}\right)\right] \tag{2}$$

$$\rho_m=\rho_v\alpha_v+\rho_l(1-\alpha_v) \tag{3}$$

$$\mu_m=\mu_v\alpha_v+\mu_l(1-\alpha_v) \tag{4}$$

where u_i is the velocity vector, p is the pressure and μ_t denotes the turbulent eddy viscosity. ρ_m and μ_m represent the mixture density and dynamic viscosity, as expressed in equations (3) and (4), respectively. The subscripts l and v denote the water and vapor phases, respectively, and α_v is the vapor volume fraction.

The delayed detached eddy simulation (DDES) is chosen to modelling turbulence flow in current study. The DES method is considered as a hybrid RANS/LES turbulence modeling approach based on the idea of modeling the boundary layer by a Reynolds-averaged Navier-Stokes (RANS) model and switching to a LES mode in detached regions. The DES approach is efficient to predict the complicated cavitation and non-cavitation flow for axial flow pump (Shen et al., 2021), propeller (Wang et al., 2021b) and PJP (Li et al., 2020) with less computational cost compared with LES method. The DDES model proposed by Spalart et al. (2006) offers limiter protection to overcome the grid-induced separation in the basic DES model, the governing equations for DDES are as follows:

$$\frac{\partial(\rho_m k)}{\partial t}+\frac{\partial(\rho_m k u_j)}{\partial x_j}=\frac{\partial}{\partial x_j}\left[\left(\mu_m+\frac{\mu_t}{\sigma_{k3}}\right)\frac{\partial k}{\partial x_j}\right]+P_k-\frac{\rho_m k^{3/2}}{l_{DDES}} \tag{5}$$

$$\frac{\partial(\rho_m \omega)}{\partial t}+\frac{\partial(\rho_m \omega u_j)}{\partial x_j}=\frac{\partial}{\partial x_j}\left[\left(\mu_m+\frac{\mu_t}{\sigma_{\omega 3}}\right)\frac{\partial \omega}{\partial x_j}\right]+\alpha_3\frac{\omega}{k}P_k-\beta_3\rho_m\omega^2 + 2(1-F_1)\rho_m\frac{1}{\omega\sigma_{\omega 2}}\frac{\partial k}{\partial x_j}\frac{\partial \omega}{\partial x_j} \tag{6}$$

The k equation of the original shear stress transport (SST) k-ω is adjusted by the l_{DDES} term in the DDES governing equations, and the ω equation remain unchanged. The l_{DDES} term stands for the length scale associated with triggering the transition from RANS mode to LES mode, which is expressed as

$$l_{DDES}=l_{RANS}-f_d\max(0,l_{RANS}-l_{LES}) \tag{7}$$

where f_d is an empirical delay function, $l_{RANS}=\sqrt{k}/C_\mu\omega$ and $l_{LES}=C_{DES}\,\Delta_{\max}$.The C_μ has a constant value of 0.09, the C_{DES} is calculated with the function: $C_{DES}=C_{DES1}\cdot F_1+C_{DES2}\cdot(1-F_1)$, where F_1 is the blending function, and the C_{DES1}, C_{DES2} have the value of 0.78 and 0.61, respectively.

2.2. Cavitation model

The Zwart (Philip J. Zwart et al., 2004) cavitation model is employed to predict the mass transfer rate between water and vapor, which can be expressed as

$$\frac{\partial(\rho_v\alpha_v)}{\partial t}+\frac{\partial(\rho_v\alpha_v u_j)}{\partial x_j}=\dot{m}^+-\dot{m}^- \tag{8}$$

The source term $\dot{m}^+$ denotes the liquid vaporization rate and $\dot{m}^-$ represents the vapor condensation rate. The source terms are built based on the Rayleigh-Plesset equation, the relevant evaporation and condensation terms are described as follows:

$$\dot{m}^+=F_e\frac{3\alpha_{nuc}(1-\alpha_v)\rho_v}{R_b}\sqrt{\frac{2}{3}\frac{|p_v-p|}{\rho_l}}\quad(p<p_v) \tag{9}$$

$$\dot{m}^-=F_c\frac{3\alpha_v\rho_v}{R_b}\sqrt{\frac{2}{3}\frac{|p-p_v|}{\rho_l}}\quad(p\geq p_v) \tag{10}$$

where the volume fraction of nuclei α_{nuc} is 5×10^{-4}, F_e and F_c are the vaporization and condensation coefficients with default values of 50 and 0.01, respectively. The bubble radius R_b is 1×10^{-6} m, p_v is the vapor saturation pressure at a local thermodynamic state.

3. Numerical setup

3.1. Test model

The test model in current study is a scaled pre-swirl stator PJP applied to an underwater vehicle. The geometry of the model is shown in Fig. 1 and the basic geometry parameters are presented in Table 1. The PJP model includes three main hydraulic components, namely an eight-bladed front stator, a six-bladed axial flow rotor and a decelerating duct. The rotor diameter is $D_r=166.4$ mm, and the hub diameter ratio is 0.3. The profiles of rotor and stator blades are designed based on NACA66 airfoil, which offers high anti-cavitation ability for propellers. The tip clearance between the rotor tip and duct inner surface is 1 mm. The axial distance between the trailing edge (TE) of stator blades and leading edge (LE) of rotor blades is $0.35D_r$. The rotating direction of rotor is right-hand and the rotation speed is $n=20$ r/s.

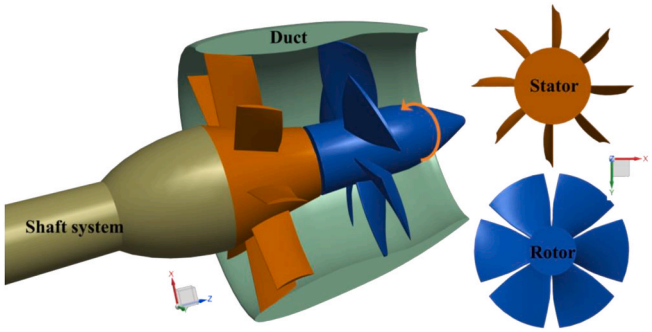

Fig. 1. Geometry of PJP model.

Some dimensionless hydrodynamic coefficients related to the PJP performance are defined as Eq. (11).

$$J=\frac{V_\infty}{nD_r},K_{Tr}=\frac{T_r}{\rho_l n^2D_r^4},K_{Qr}=\frac{Q_r}{\rho_l n^2D_r^5},\eta_r=\frac{J}{2\pi}\frac{K_{Tr}}{K_{Qr}},\sigma=\frac{p_{in}-p_v}{0.5\rho_l n^2D_r^2} \tag{11}$$

where J is the advance coefficient, the V_∞ is the uniform oncoming velocity; T_r is the thrust, and Q_r is the torque. K_{Tr} and K_{Qr} represents the thrust and torque coefficients of the rotor, respectively. η_r denotes the efficiency of rotor. σ is the dimensionless cavitation number, p_{in} is the specified ambient pressure.

3.2. Computational domain and mesh details

Fig. 2 shows the computational domain of the PJP model. The whole computational domain consists four parts: the rotor domain, the stator domain, the near field domain and the far field domain. The size of far field domain is $16D_r\times3.6D_r\times3.6D_r$, which is consistent with the experimental cavitation tunnel. The near field domain is separated out for a better layout of the grid in order to capture the wake field details, it is set as a cylinder with a length of $5.5D_r$ and a diameter of $2D_r$.

The separated computational domains of PJP are discretized by hexahedral structured grids, as shown in Fig. 3. The girds of rotor and stator are first set up on the single blades and then the complete ones are obtained by periodical copying, respectively. The O-block topological structures are employed around rotor and stator blades and also duct surface, so that the boundary layer grids can be easily arranged. The grid of 1 mm tip clearance between the rotor and the duct is refined to well simulate the tip leakage flow, as shown in Fig. 3(a). The grid is also refined in some regions of near field domain to further capture the wake vortices, as observed in Fig. 3(b). Three grid schemes are set to carry out grid independent test. The grid numbers for coarse, medium and fine grid schemes are 4.98 million, 9.38 million, 20.18 million, respectively. The grid number details of sub-domains are shown in Table 2. The grids for rotor tip clearance are set as 30, 25 and 15 layers for fine, medium and coarse grid schemes. The height of the first layer of grid near the wall surface is carefully set to ensure the average y+ is below 5 for three grid schemes. Table 3 shows the results of grid independence test. The hydrodynamic coefficients K_{Tr} and K_{Qr} for PJP are calculated at $J=0.6$ and $J=1.0$ non-cavitation conditions based on three grid schemes. According to the procedure for estimate the uncertainty of grid discretization in computational fluid dynamics (CFD) proposed by Celik et al. (I.B. Celik et al., 2008), the approximate relative error e_a^{21}, extrapolated relative error e_{ext}^{21} and grid convergence index GCI_{fine}^{21} for fine grid scheme are presented in Table 3. It is observed that all error estimates are within 3%, which fully meet the simulation requirement. Finally, the fine grid scheme with 20.18 million nodes is selected for the

Table 1
Pre-swirl stator PJP parameters.

Scale ratio λ	20	Rotor blade number	6
Rotor rotation speed n	20 r/s	Stator blade number	8
Rotor diameter D_r	166.4 mm	Rotor-stator spacing	$0.35D_r$
Hub diameter ratio	0.3	Rotation direction	Right-handed
tip clearance	1 mm	Airfoil type	NACA66

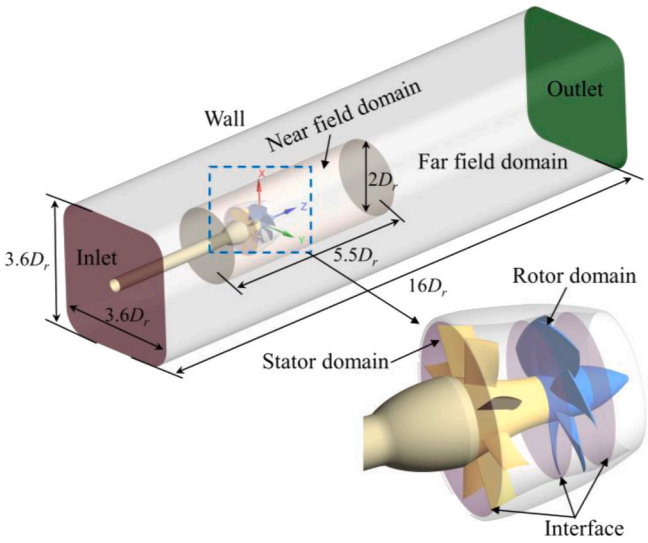

Fig. 2. Computational domain of PJP.

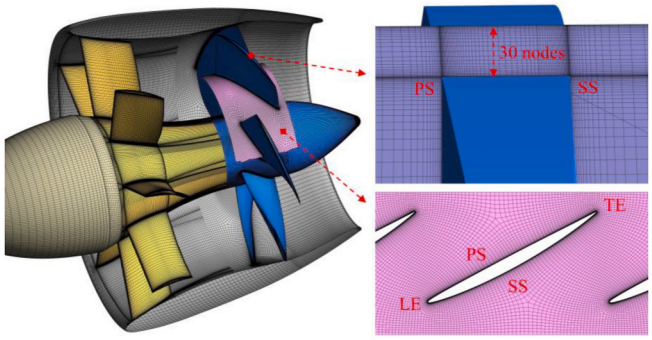

(a) Mesh details of stator, rotor and duct.

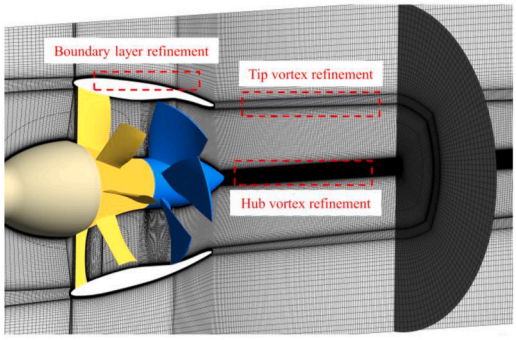

(b) Mesh details of PJP wake field.

Fig. 3. Mesh details of computational domain.

Table 2
The grid number details of PJP (million).

Mesh scheme	Rotor domain	Stator domain	Near field domain	Far field domain	Total number
Coarse	2.09	0.88	1.48	0.53	4.98
Medium	3.30	1.97	2.99	1.12	9.38
Fine	6.18	3.68	9.20	1.12	20.18

following simulations in this study. Fig. 4 presents the y + distributions of PJP for the fine grid scheme. The average y + for rotor blade, stator blade and duct surface are 2.6, 2.8 and 1.8, respectively.

3.3. Calculation setting

The uniform velocity V_∞ is set for the inlet with the constant value equals to 3.328 m/s, corresponding to the design advanced coefficient $J = 1.0$. The static pressure is set as the outlet boundary condition, the different cavitation numbers can be obtained by changing the outlet static pressure, as described in Eq. (11). All the solid surfaces, such as the rotor blades and duct surface, are defined as no slip wall. The rotor domain is defined as a rotating domain with fixed rotation speed $n = 20$r/s. The cavitating flow is firstly simulated by SST k–ω turbulence model and Zwart cavitation model to obtain a steady state result as the initial flow field for the unsteady cavitation simulations. Then, the unsteady cavitation simulations are carried out by employing DDES method. The time step for the unsteady simulation is set as 1.39×10^{-4} s, which corresponds to the time for rotor to rotate one degree. The maximum number of inner iterations is 20 per time-step with a 10^{-5} root mean square (RMS) residual criterion. The duration of the cavitation simulation lasts for 8 rotating cycles, and the data of last 5 cycles are used to conduct the time-dependent analysis.

3.4. Validation of simulation

The hydrodynamic and cavitation performance of the PJP model is tested in a water tunnel of the Science and Technology on Water Jet Propulsion Laboratory, the Marine Design and Research Institute of China. Fig. 5 illustrates the hydrodynamic performance curves obtained from experimental tests and numerical simulations. It is observed that the thrust coefficient K_{Tr} and torque coefficient K_{Qr} obtained from the numerical simulations are lower than the experimental measurements under six operating conditions, the K_{Tr} and K_{Qr} keep decrease with the increase of advanced coefficient J, the rotor efficiency η_r increases as J increases. The trends of hydrodynamic performance curves obtained from experiments and numerical simulations are in good agreement. The maximum relative errors between experiments and numerical simulations for K_{Tr}, K_{Qr} and η_r are 8.1%, 7.5% and 1.5%, respectively. The numerical methodology employed in current study is available to analyze the hydrodynamic performance of PJP. Moreover, the cavitation experiments of the PJP are also carried out in water tunnel. The high-speed visualizations of cavitation patterns are carried out at $J = 0.6$, $n = 25$r/s under different cavitation numbers. The cavitation pattern obtained by high-speed imaging at $\sigma = 2.0$ is selected to compare with the numerical results under the same operating condition. Fig. 6 shows the typical cavitation structures of experiment and iso-surface of $\alpha_v = 0.1$ at $\sigma = 2.0$. It can be seen that the cavitation mainly occurs around the tip region of rotor blade at this cavitation condition, including tip clearance cavitation, shear layer cavitation and tip leakage vortex (TLV) cavitation, which are all captured both in the experiment image and numerical simulation result, as labelled 1, 2 and 3 in Fig. 6. Therefore, the cavitation patterns obtained from the numerical simulation is in general agreement with the experiment in terms of intensity and distribution, which demonstrates that the cavitation simulation method adopted in this study is reliable for subsequent analysis.

4. Results and discussion

4.1. Cavitation patterns at different conditions

The cavitation simulation is carried out at two typical cavitation stages, including a light cavitation condition $\sigma = 3.5$ and a heavy cavitation condition $\sigma = 2.2$. The heavy cavitation condition is considered to analyze the effects of cavitation on hydrodynamic loading and vortex development, and cavitation-vortex interaction. The light cavitation condition is selected as a reference for the comparative analysis, and is also used to investigate the cavitation incipient of rotor under tip unloading treatment. Fig. 7 illustrates the instantaneous cavitation patterns within the rotor domain at these two cavitation stages through

Table 3
Details of grid independence test.

J	Φ	φ_1 (fine)	φ_2(medium)	φ_3(coarse)	e_a^{21}	e_{ext}^{21}	GCI_{fine}^{21}
0.6	K_{Tr}	0.5715	0.5791	0.5811	1.32%	0.76%	0.95%
	K_{Qr}	0.0964	0.0969	0.0971	0.59%	0.25%	0.32%
1.0	K_{Tr}	0.4663	0.4624	0.4555	1.06%	2.06%	2.63%
	K_{Qr}	0.0825	0.0821	0.0813	0.59%	0.80%	1.01%

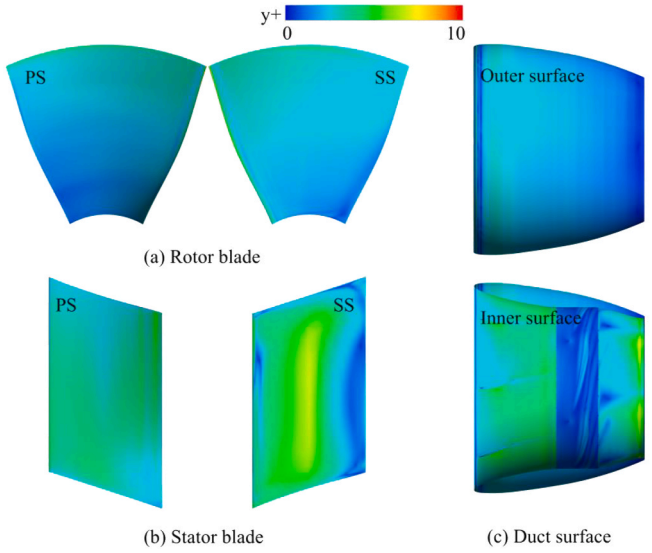

Fig. 4. The y + distributions on rotor, stator and duct surfaces.

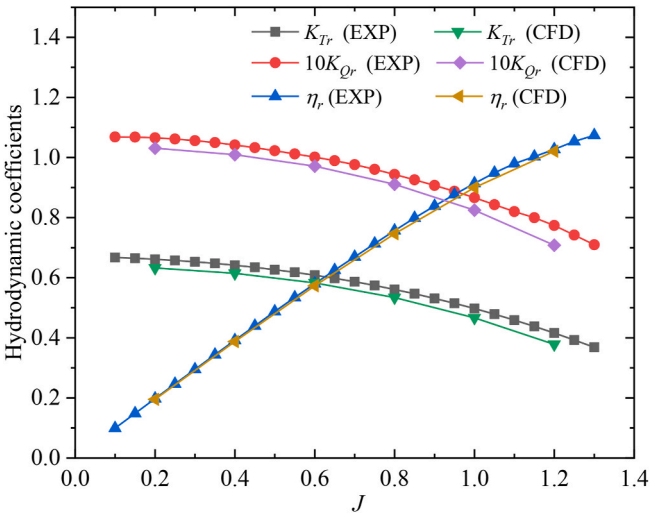

Fig. 5. Hydrodynamic performance curves of PJP.

the iso-surface of $\alpha_v = 0.1$. The blade chord ratio λ is defined to describe the specific locations where the cavity is formed, where $\lambda = 0$ and $\lambda = 1$ is respectively located at the LE and TE of the blade tip, and $\lambda = 0.5$ is located at the midpoint of the tip chord. It is found that the tip clearance cavitation, TLV cavitation and blade sheet cavitation are both observed in light and heavy cavitation conditions. At the light cavitation condition, the sheet cavitation occurs at the LE of the blade SS near the hub surface and distribution patterns are quite different on adjacent blades. As Fig. 7(a) shows, the cavities are not equally distributed on blades 1, 2, 3, and also blades 4, 5, 6, while the cavities on blades 1 and 4, blades 2 and 5, blades 3 and 6 seem to be more similar. The wake flow of pre-swirl stator with strong spatial non-uniformity and temporal

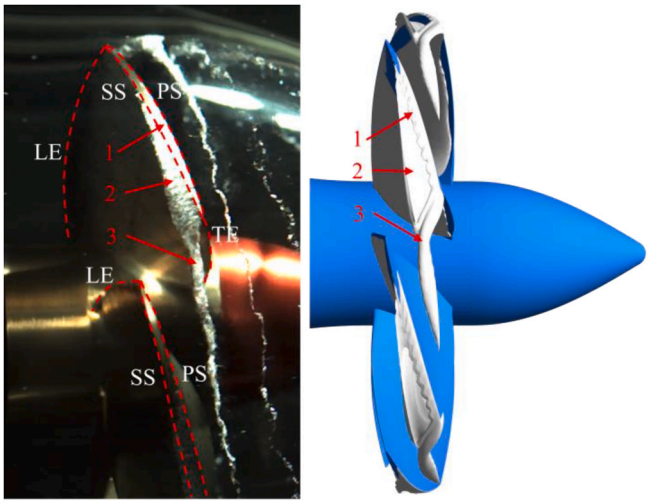

Fig. 6. Cavitation patterns obtained from experiment and simulation.

unsteadiness disturbs the sheet cavitation patterns by changing incidence angles of rotor blade. Due to the phase difference between blades of stator and rotor, the sheet cavities on adjacent blades suffer from different degrees of interaction with the wake flow of each stator blade, which further causes the non-uniform distribution of sheet cavities on adjacent blades (Zhao et al., 2021a, 2021b). In current study, rotor blades 1 and 4 are in equivalent phases with regard to their relative position towards the stator blades, as well as blades 2 and 5, blades 3 and 6. It largely explains the phenomenon of cavities being similarly distributed on the rotor blades with a phase difference of 180°.

At the light cavitation stage, the tip clearance cavitation is found at the rotor tip where $\lambda > 0.5$ due to flow separation occurs when the tip flow passes the right angle near the PS (Zhang et al., 2015b). The TLV cavitation occurs slightly around the core region of TLV where the local pressure is below the saturation vapor pressure. The tip clearance cavitation and TLV cavitation are not disturbed by phase effects. At the heavy cavitation stage as shown in Fig. 7(b), the sheet cavitation expands along the radial direction, covering the most of blade SS, and the distribution of cavities still show great difference in adjacent blades, following the same rules summarized from the light cavitation stage $\sigma =$ 3.5. The TLV cavitation also gets more aggressive, with the incipient location moving forward to $\lambda = 0.5$ and gradually mixing with tip clearance cavitation. It can also be observed delicately that the incipient positions of cavitation around the blade tip are effectively delayed even in heavy cavitation stage and that the sheet cavitation is rare at the LE near the blade tip. This cavitation pattern is quite different from other reported axial impellers in PJP (Zhao et al., 2021b), waterjet pumps (David Y. Tan et al., 2012b) as well as conventional axial flow pumps (Zhang et al., 2015b). The unloading treatment is technically carried out around the blade tip region by modulating the distribution of spanwise circulation for the purpose of delaying the cavitation inception during actual PJP operation. This is clearly elucidated in the subsequent hydrodynamic load analysis.

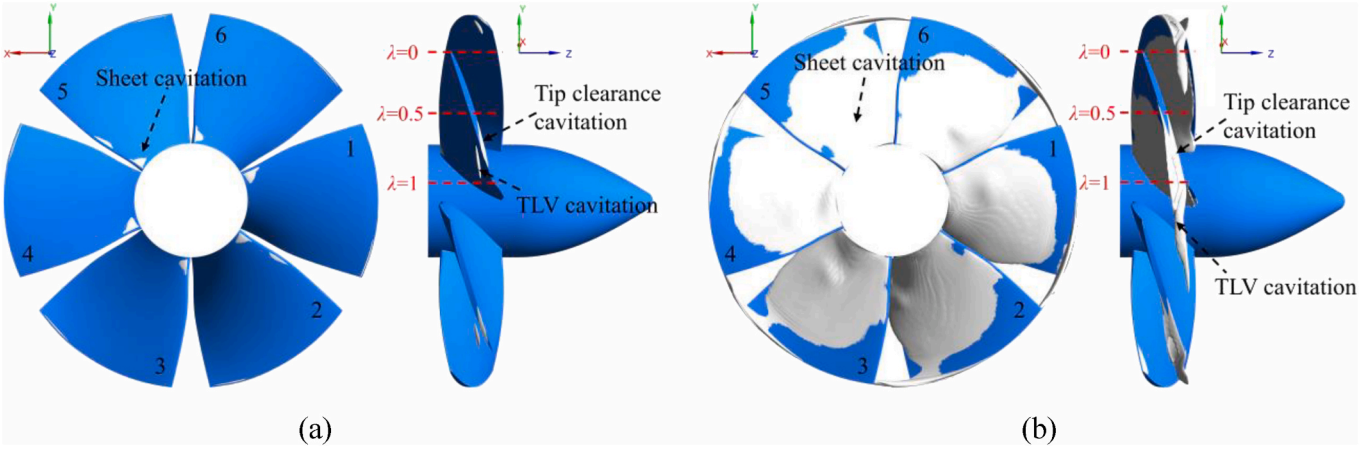

Fig. 7. Cavitation patterns at different σ identified by iso-surface of $\alpha_v = 0.1$. (a) $\sigma = 3.5$; (b) $\sigma = 2.2$.

4.2. *Effects of cavitation on hydrodynamic loading of rotor*

The hydrodynamic loading characteristics in different cavitation conditions are analyzed. Figs. 8 and 9 show the time-dependent thrust of rotor at $\sigma = 3.5$ and $\sigma = 2.2$ within one rotating cycle, respectively. The thrust of rotor is contributed by the pressure and viscous forces, they are presented separately to know the effects of cavitation on them. The non-dimensional coefficients of pressure and viscous forces are defined as $K_{Tr,p}$ and $K_{Tr,v}$, and their average values over the one rotating period are identified by the red dot line. As Fig. 8 shows, both the pressure force and viscous force fluctuate regularly at $\sigma = 3.5$. The average values of pressure and viscous forces are 0.4638 and −0.00991, respectively. The pressure force is two orders of magnitude higher than the viscous force, and the viscous force is negative. At heavy cavitation stage $\sigma = 2.2$, the pressure and viscous forces fluctuate more dramatically due to the unsteady evolution of cavitation, the average values of them are 0.3641 and −0.00733, respectively. Compared to the light cavitation stage, the pressure force decreases significantly owing to the attached sheet cavity on SS blocks the blade passage (Tan et al., 2015), resulting in the reduction of working capacity of rotor. However, the loading contributed by viscous force is substantially reduced when cavities cover the most of blade SS. The thrust performance of rotor shows breakdown in the heavy cavitation stage.

The thrust loading of rotor at different cavitation conditions are also presented in the frequency domain, as shown in Fig. 10. The frequency domain curves are obtained by Fast Fourier Transform (FFT) approach based on stable time-dependent thrust data in last 5 cycles. The frequency f in Fig. 10 is normalized by f_{BPF}, where f_{BPF} is the blade passing frequency of rotor and equals to 120Hz. The f_s represents the blade passing frequency of pre-swirl stator, which equals to the shaft frequency ($f_n = 20$Hz) times the number of stator blades, that is $f_s = 160$Hz. Analysis of Fig. 10(a) reveals that the f_{BPF} and its multiples are the dominant frequencies at light cavitation condition $\sigma = 3.5$. The maximum amplitude is located at $4f_{BPF}$ ($f = 480$Hz). This is regards as the rotor-stator resonance phenomenon due to an even number of stator and rotor blades concurrently (Qin et al., 2022). At the heavy cavitation condition $\sigma = 2.2$, it is observed that the dominant frequencies shift to the f_s and its multiples. The thrust spectrum shows obvious broadband characteristic with overall increased amplitude. The rotor-stator resonance phenomenon still obvious at $f = 480$Hz, the amplitudes at $2f_s$, $4f_s$, $5f_s$, $6f_s$, $7f_s$, as well as in low frequency range (below the f_{BPF}) increase significantly. The sheet cavitation covers most of the blade SS at $\sigma = 2.2$ as mentioned before, the unsteady developing of cavities enhances the thrust pulsation. In addition, the increasing sheet cavity suffers from the perturbation of the stator wake, the cavity on each blade SS constantly sweeps the wake flow of stator and interacts with stator trailing vortices, which causes the change of dominant frequencies of thrust spectrum to f_s and its multiples (Zhao et al., 2021b).

The unsteady thrust of each rotor blade under different cavitation conditions are also shown in Fig. 11. The thrust of each single blade is normalized to $K'_{Tb} = K_{Tb}/\overline{K_{Tb}}$, where K_{Tb} is the time-dependent thrust coefficient for a single blade, $\overline{K_{Tb}}$ is the time average value within the selected sampling interval. It is obvious that the thrust of single blades for the light cavitating case performs in a perfect sinusoidal pattern. The thrust curves of each two blades with the same phase coincide perfectly and fluctuate regularly. However, the single blade thrust presents more irregularly at heavy cavitation stage $\sigma = 2.2$. The unsteady developing of cavities on different single blade under the perturbation of non-uniform pre-swirl stator wakes dominants this phenomenon. The irregular and uneven fluctuations in blade thrust not only increase the excitation level of the rotor blades, but also lead to random vibrations in the propulsion shafting system. Fig. 12 shows the frequency domain curves of the blade thrust K_{Tb}. For the single blade, the f_s and its multiples dominant the frequency characteristics in both light and heavy cavitation conditions. Specially, the frequency domain curves for heavy cavitating case contain

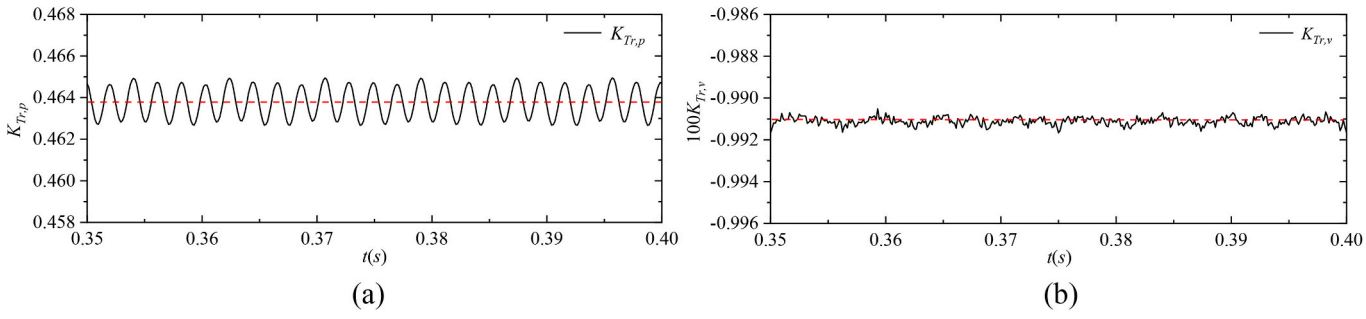

Fig. 8. The unsteady thrust contributed by pressure and viscous forces at $\sigma = 3.5$. (a) pressure force; (b) viscous force.

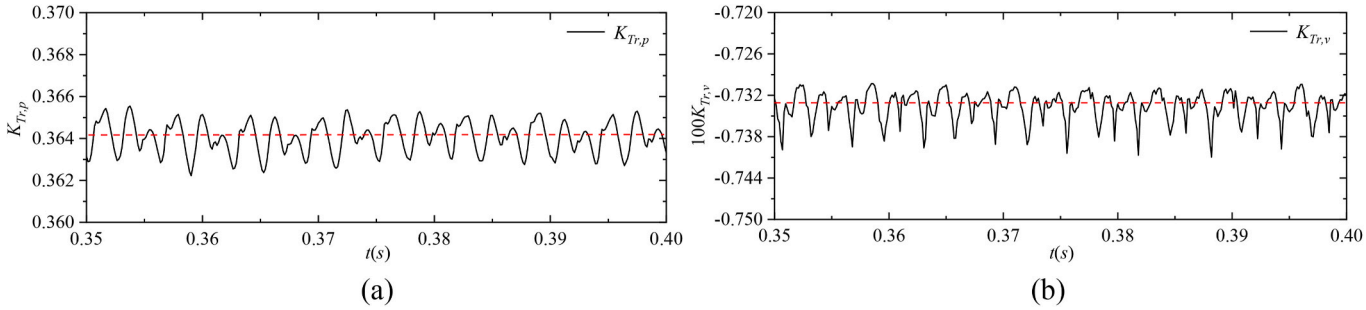

Fig. 9. The unsteady thrust contributed by pressure and viscous forces at $\sigma = 2.2$. (a) pressure force; (b) viscous force.

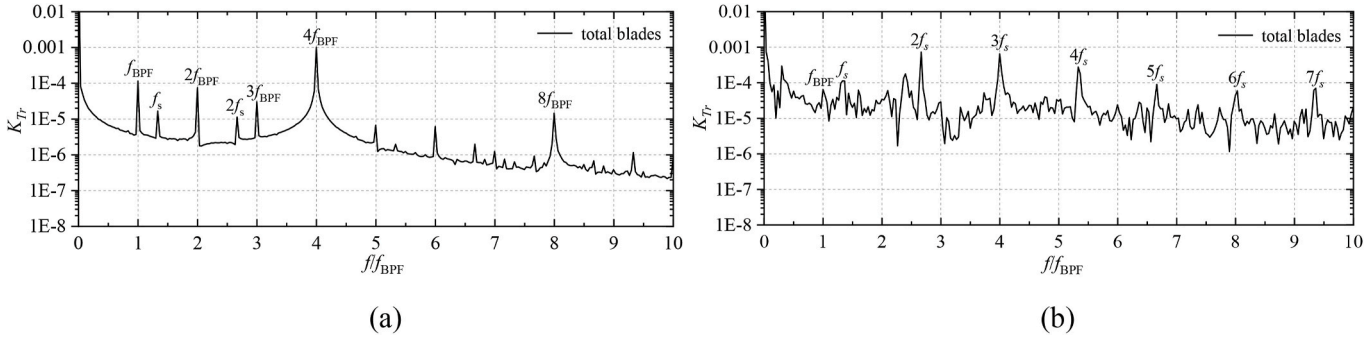

Fig. 10. Frequency domain curves of the rotor thrust at different cavitation conditions. (a) $\sigma = 3.5$. (b) $\sigma = 2.2$.

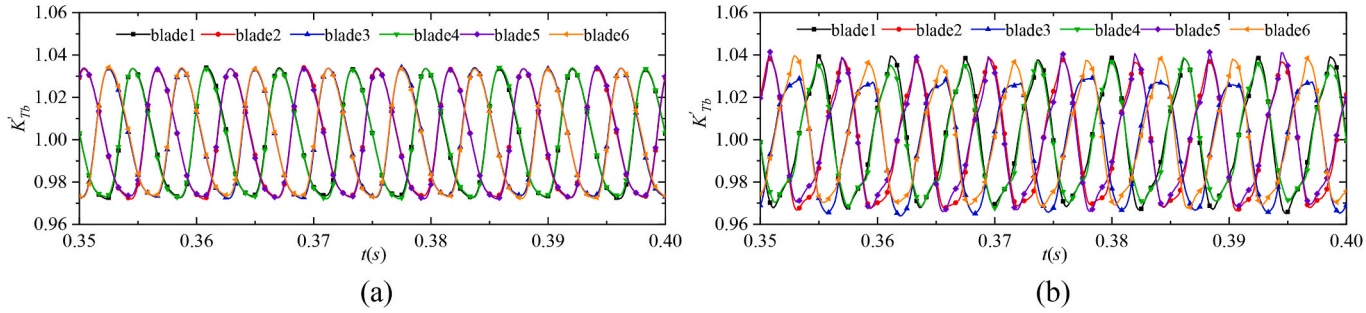

Fig. 11. Frequency domain curves of thrust for single blade at different cavitation conditions. (a) $\sigma = 3.5$. (b) $\sigma = 2.2$.

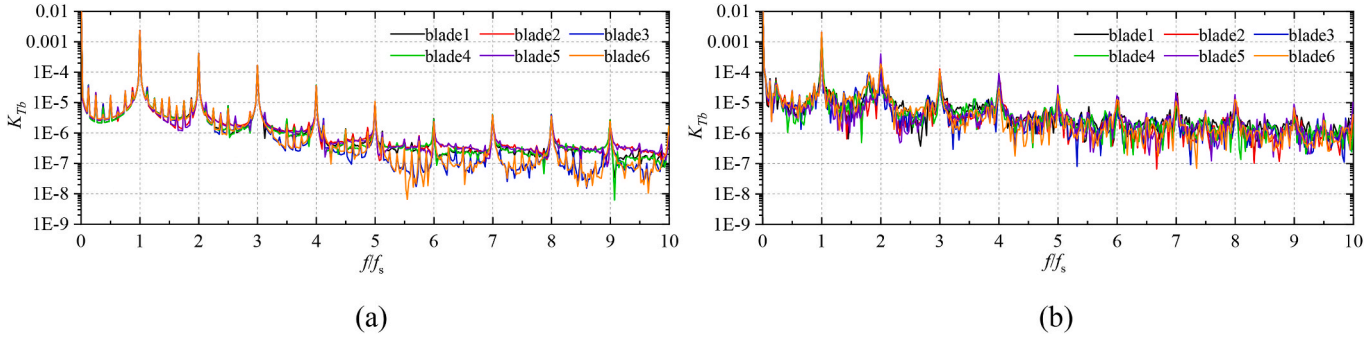

Fig. 12. Time domain curves of thrust for single blade at different cavitation conditions. (a) $\sigma = 3.5$. (b) $\sigma = 2.2$.

obvious broadband components which spanned over a wide frequency band.

Fig. 13 shows the distribution of pressure fluctuation intensity (I_{PF}) on the rotor blade to know the potential reasons for thrust pulsation at different cavitation stages. The I_{PF} is defined by the standard deviation of time-dependent pressure in a certain time period (Tan and Sun, 2020), the related expression are as follows:

$$\overline{p} = \frac{1}{N}\sum_{i=1}^{N} p_i, I_{PF} = \sqrt{\frac{1}{N}\sum_{i=1}^{N}(p_i - \overline{p})^2}, C_{IPF} = \frac{I_{PF}}{0.5\rho_l n^2 D_r^2} \tag{12}$$

where $\overline{p}$ is the arithmetic average of pressure, N is the sampling number

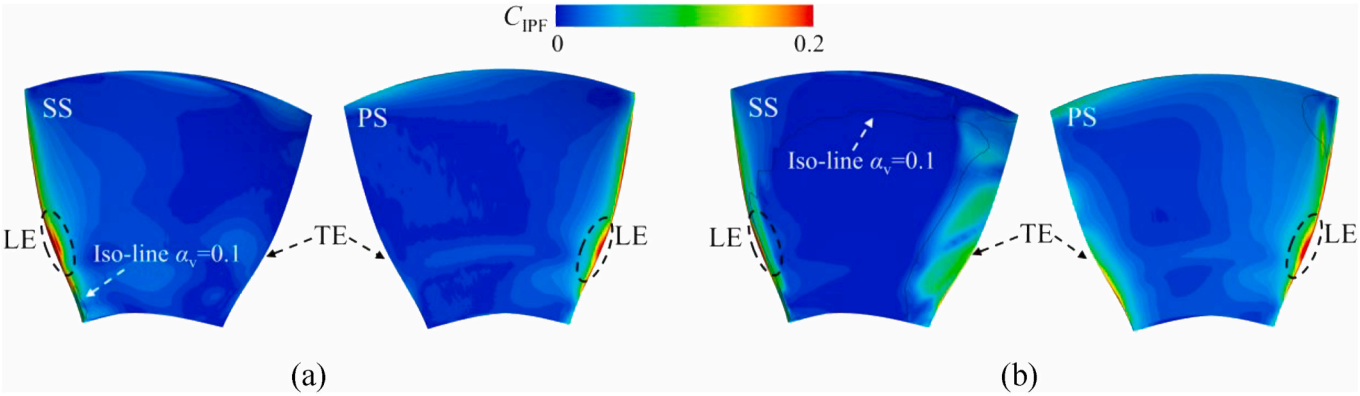

Fig. 13. Pressure pulsation intensity on rotor blade. (a) $\sigma = 3.5$, (b) $\sigma = 2.2$.

and equals to 720 in this study, that is two stable rotating cycles, p_i is the pressure on grid nodes at each time step. The dimensionless coefficient of pressure fluctuation intensity C_{IPF} is used for further analysis. It is observed from Fig. 13 that the higher C_{IPF} values present around the LE of rotor blade both in light and heavy cavitation conditions, especially in the region marked by the black dashed ellipse. The dynamic variations of the blade incidence angle due to temporal unsteadiness of the pre-swirl wake flow is the underlying reason for the large pressure fluctuations on the blade LE. For the marked regions, the interaction between the strong root trailing vortex of stator blade with rotating rotor causes its violent pressure pulsation. It is also found that the C_{IPF} is higher at the blade TE at heavy cavitation stage $\sigma = 2.2$, while it is not obvious at $\sigma = 3.5$. The thicken sheet cavitation at $\sigma = 2.2$ induces the vortex shedding at the TE and therefore increase the pressure pulsation over there. This further clarifies that the cavitation, vortices, and their interaction are the core sources in inducing an increased hydrodynamic excitation of rotor blades.

Lastly, in order to understand the contribution of different parts of the rotor blades to the thrust breakdown at different cavitation stages, the entire single blade is split into 10 parts in the radial direction according to the span coefficients to reflect local thrust loss. It is noted that the force loaded on each single blades of rotor is slightly different owing to the non-uniform wake flow of the front stator and the non-synchronous development of sheet cavitation on blade surface, as presented in Fig. 11. Here we mainly focus on the general spanwise distribution of the loading on single blade, so the differences in loading between different blades can be ignored, and the blade 1 is chosen for detailed analysis. The thrust and torque generated by each part is recorded, and Eq. (13) (Ji et al., 2021) is employed to obtain the non-dimensional loading values per unit area.

$$\Delta K_{Tb} = \frac{\Delta T_b}{\rho n^2 D_r^2 \Delta S}, \ \Delta K_{Qb} = \frac{\Delta Q_b}{\rho n^2 D_r^3 \Delta S} \tag{13}$$

where ΔT_b and ΔQ_b are the thrust and torque of each part for a single blade, respectively. ΔS is the area of each part. Fig. 14 shows the spanwise distribution of ΔK_{Tb} and ΔK_{Qb} at two different cavitation stages. The ΔK_{Tb} and ΔK_{Qb} increase gradually along the radial direction and finally decrease near the tip region. This is ascribed to the technical unloading treatment for the blade tip region, as previously mentioned. At $\sigma = 2.2$, the ΔK_{Tb} and ΔK_{Qb} maintain the trend of increasing firstly and then decreasing in the radial direction. Their values decrease to some extent at different spans with different magnitudes compared to the values at $\sigma = 3.5$. The loading near the blade hub region contributes less to the overall thrust reduction because of the weaker work capability.

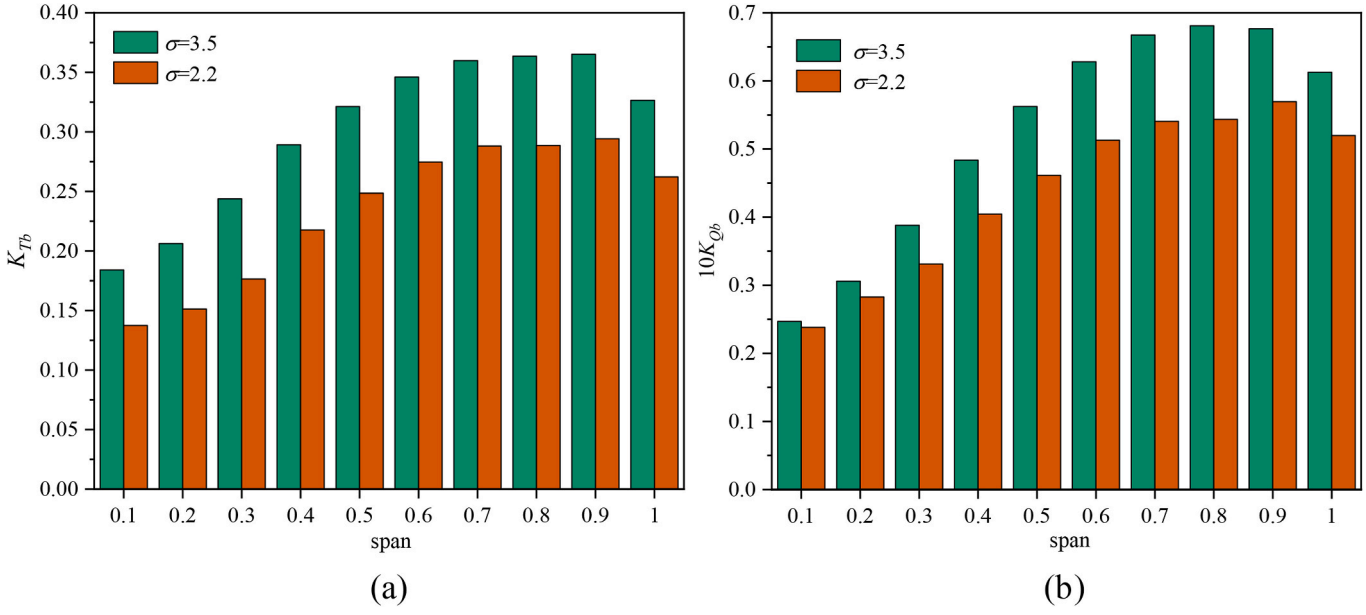

Fig. 14. Spanwise distribution of thrust and torque coefficients for single rotor blade.

4.3. Effects of cavitation on TLV evolution

4.3.1. TLV morphology in the incipient stage

The TLV is considered to be one of the main vortex structures in the PJP as it will extend to the far wake field under mainstream driving (Li et al., 2021). It originates from the rollup of a multi-layered tip leakage flow, and propagates within the rotor passage towards the neighboring blade (Tan et al., 2012a). Its evolving characteristics in the PJP are different from those in the conventional axial flow pump and opened propeller. To well investigate the effects of cavitation on the evolution of TLVs and their interaction, the morphology of TLVs in the incipient period and the fully developed state in the wake field are successively analyzed at different cavitation conditions. Fig. 15 shows the pressure distribution over different slices in the TLV forming regions, the pressure is normalized by $C_P = (p - p_0)/0.5\rho_l n^2 D_r^2$, where $p_0 = 101325$Pa. The cavitation regions are also shown by the iso-surface of $\alpha_v = 0.1$. The trajectories of the TLV are identified by red dot curves connecting the lowest pressure points at the vortex cores on different slices. It is found in Fig. 15 that the incipient trajectory of the TLV is somewhat different at different cavitation stages. At the heavy cavitation condition $\sigma = 2.2$, the incipient trajectory of the TLV is more distorted and moves closer to the SS before departing the blade, which is also as evident from TLV streamlines in Fig. 16. The incipient locations of the TLVs at $\sigma = 3.5$ and $\sigma = 2.2$ are essentially the same as the loading condition is constant. However, the strength of the TLVs seem to be different as seen from the apparent size of the streamlines in Fig. 16.

Fig. 17 shows the vorticity distribution for slices I ~ IV at different cavitation stages. The vorticity magnitude is normalized by D_r and V_∞. It is observed that the TLV is clearly identified by the large-scale vorticity area. The backflow with high vorticity interacts with the main flow and eventually rolls up into the TLV. At slice I and II, TLV1 is initially formed from own blades and has similar shape and intensity under different cavitation stages. However, the intensity of TLV2 from prior adjacent blade is higher at heavy cavitation stage. Moreover, the TLV1 appears to be slightly deformed under interaction with cavities at slice III under heavy cavitation stage. At slice IV, the TLV1 is noticeably stronger under $\sigma = 2.2$. The intensity of the TLV increases after interaction with large scale cavities. This is in accordance with the streamlines shown in Fig. 16. Subsequently, the relative vorticity transport equation is adopted to further elucidate the underlying mechanism of cavitation-vortex interaction.

The relative vorticity transport equation is obtained by taking curl operation on both sides of the fluid momentum equation in differential form (Ji et al., 2014). It is currently being used to analyze the interaction mechanism between vortices and cavitation both in hydrofoils and hydraulic machineries (Fei et al., 2022; Liu et al., 2019; Sun et al., 2021). Here, it is utilized to investigate the interaction between TLV and its induced cavitation in the PJP and the underlying reasons for the enhancement of TLV intensity in heavy cavitation stage. The exact equation is shown as follows:

$$\frac{D\vec{\Omega}_R}{Dt} = \left(\vec{\Omega}_R \cdot \nabla\right)\vec{W} - \vec{\Omega}_R\left(\nabla \cdot \vec{W}\right) - 2\nabla \times \left(V_a \times \vec{W}\right) + \frac{\nabla\rho_m \times \nabla p}{\rho_m^2} + (\nu_m + \nu_t)\nabla^2\vec{\Omega}_R \tag{14}$$

where $\vec{\Omega}_R$ is relative vorticity, V_a is angular velocity, ρ_m is mixture density, $\vec{W}$ is relative velocity, and ν_m is kinematic viscosity and ν_t is turbulent viscosity.

In Eq. (14), $\frac{D\vec{\Omega}_R}{Dt}$ is the variation rate of relative vorticity. The first four terms on the right side are the stretching, dilatation, Coriolis force and baroclinic torque terms, respectively. The stretching term represents the influence of the velocity gradient on the vortex evolution. The dilatation term is affected by the expansion and contraction of fluid elements. The Coriolis force term describes the effect of Coriolis force on the vorticity generation, which is resulted from the rotor rotation. The baroclinic torque term denotes the effect of pressure and density gradients on the vortex. The last term is viscous diffusion term, which represents the influence of viscous diffusion. As the TLV in PJP shows strongly turbulent features with a high Reynolds number, the viscous effect is ignored in the following analysis.

Figs. 18 and 19 shows the distributions of the stretching, dilatation, Coriolis force and baroclinic torque terms at four slices under $\sigma = 3.5$ and $\sigma = 2.2$, respectively. As seen from Figs. 18(a) and 19(a), the stretching term has a larger value in the TLV generation region, as evident from TLV1 of own blade and TLV2 from adjacent blade. Its intensity is higher at $\sigma = 2.2$ due to the increased cavitation-vortex interaction. The high values of dilatation term are mainly displayed in

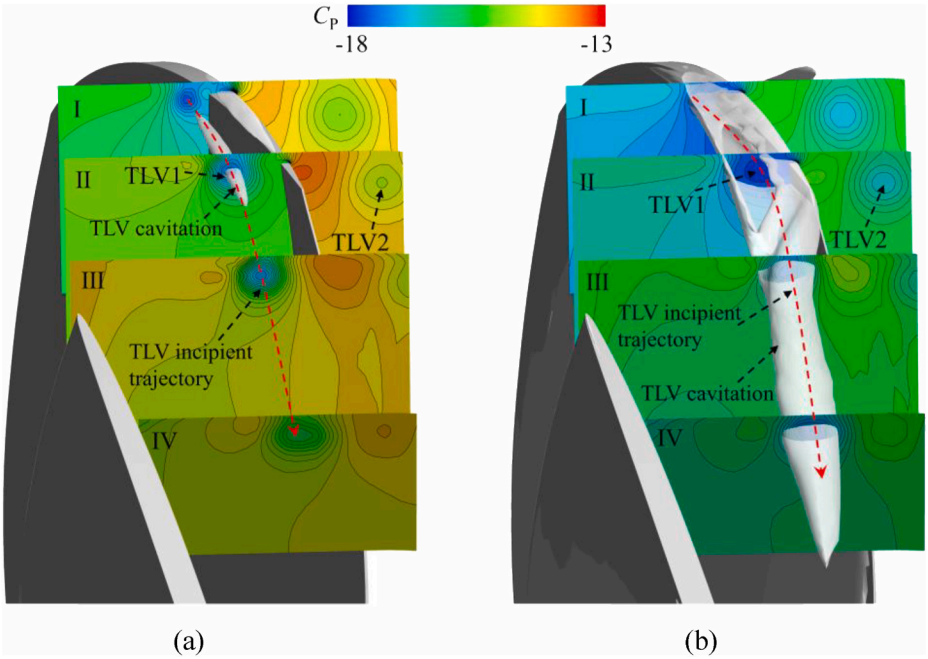

Fig. 15. The TLV incipient patterns at different cavitation stages. (a) $\sigma = 3.5$, (b) $\sigma = 2.2$.

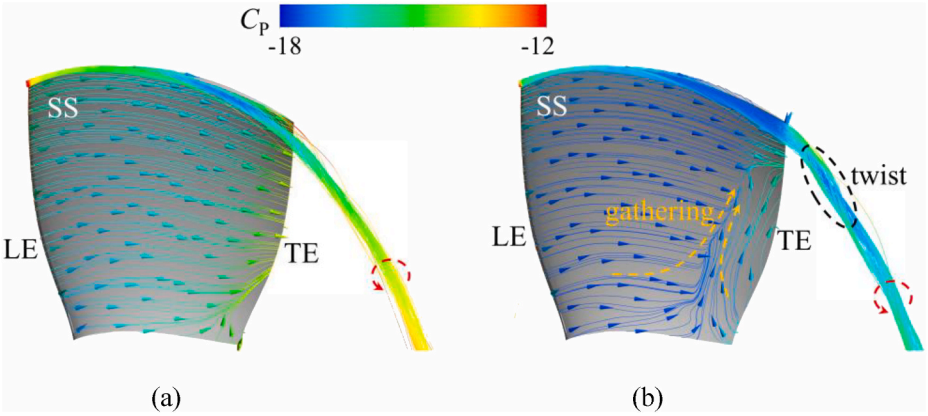

Fig. 16. The streamlines of TLV trajectory and surface streamlines at blade SS. (a) $\sigma = 3.5$, (b) $\sigma = 2.2$.

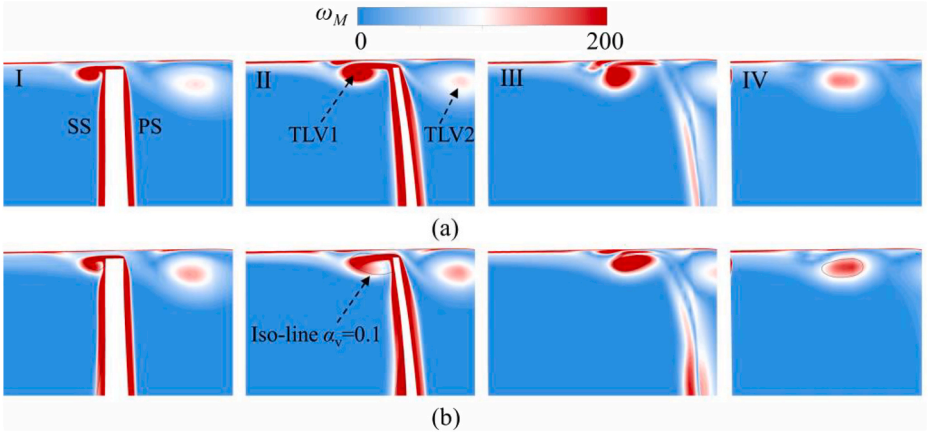

Fig. 17. The vorticity distribution on different slices. (a) $\sigma = 3.5$, (b) $\sigma = 2.2$.

the cavity region, and it is more visible $\sigma = 2.2$. The effects of the Coriolis force term on TLV are relatively weak, which is more noticeable around the near wall region and wake of blade. The baroclinic torque term shown in Figs. 18(d) and 19(d) is mainly concentrated near the interface of liquid and vapor, which could be ignored at light cavitation stage $\sigma =$ 3.5. Comparison of these four terms indicates that the stretching term is dominant during the evolution of the TLV both in light and heavy cavitation conditions. The contribution of the dilatation and baroclinic torque terms to the vorticity transport of TLV cannot be ignored especially when cavitation is severe. By comparing with light cavitation case, the cavitation around the tip region could promote the vorticity production of TLV at the incipient stage and probably increases its intensity in downstream development.

4.3.2. TLV morphology in the wake field

The effect of cavitation on the evolution of TLV in the wake field is investigated. Fig. 20 shows the contours of pressure, velocity, and vorticity at the $x = 0$ plane for two different cavitation conditions. The vortex cores of the TLV identified by the low pressure region are marked by the red dotted circles in pressure field. It is observed from pressure field that the regions over which TLV passes show a noticeable low pressure compared to the surroundings and finally fades into the far flow field. The trajectories of the vortex cores fluctuate along the radial direction at $\sigma = 2.2$. For velocity field, although the group of secondary vortices is found behind the duct outlet at $\sigma = 3.5$, the flow in the mixing region of the main wake region and freestream is more stable. For vorticity field, it can be seen that the mutual interference between adjacent TLVs is stronger at $\sigma = 2.2$. Combining the pressure field, velocity field and vorticity field, it is suggested that the TLV appears to be more unstable in the wake field under heavy cavitation stage $\sigma = 2.2$. Regarding the instability development of the TLV in the wake field, there are many contributing reasons for this. Felli et al. (2011) conducted a series of experiments with propellers and noted that the instability of tip vortices may be more correlated to spiral-to-spiral distance between adjacent tip vortices, which belongs to mutual-inductance mode of instability which is theoretically proposed by Widnall (1972). Kumar et al. (Kumar and Mahesh, 2017) performed LES to investigate the wake instabilities of a five-bladed marine propeller and found that the interaction between some smaller vortices generated by the roll-up of the blade trailing edge wake and tip vortex of the adjacent blade is the preferred mechanism to cause instability of tip vortices. It can also be concluded from their research that the actual mechanism for the unstable evolution of tip vortices is dependent on the rotor geometry itself as well as the operating condition. Moreover, for the ducted-type propellers, the special duct-induced vortex could interact with the tip vortices and thereby affect its evolution and stability (Gong et al., 2018; Qin et al., 2021b).

In order to gain a clearer understanding on the effects of cavitation on TLV development in the wake field, the vortex structures in wake field are identified by the iso-surface of the Q-criterion ($Q = 5000s^{-2}$), as shown in Fig. 21. The TLV develops in a spiral downstream driven by the high velocity axial flow out of the duct, and its morphology is quietly different in light and heavy cavitation condition.

At $\sigma = 3.5$, the duct shear vortex is extensively present on the external surface of the duct, it sheds from the trailing edge of the duct, then merges with the outflowing TLV and eventually promotes the generation of the secondary coherent vortex structures, which is also obvious in Fig. 20. The TLV flowing from the duct shows slight

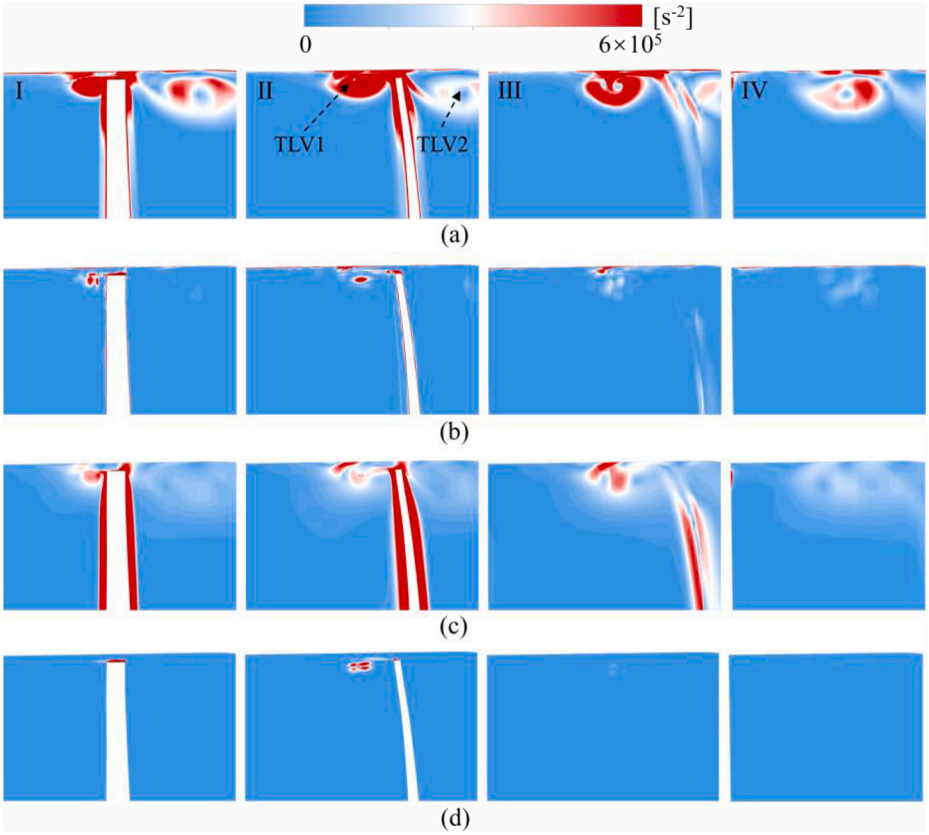

Fig. 18. The different terms of vorticity transport equation on different slices at $\sigma = 3.5$. (a) stretching term, (b) dilatation term, (c) Coriolis force term, (d) baroclinic torque term.

sinusoidal fluctuation along the spiral trajectory, as marked by the red dashed ellipse, which is ascribed to short-wave instability of tip vortices (Felli et al., 2011). Qin et al. (2021b) concluded that this phenomenon in pre-swirl stator PJP is specially induced by the pre-swirl stator, by comparing the wake vortex structures of PJP with and without stator under the same operating condition. We further observed that the sinusoidal displacements exhibit 8 periods (8 crests and 8 troughs) during the single TLV develops one rotation (360°) along the spiral path, this is consistent with the number of stator blades which further supports the conclusion proposed by Qin et al. (2021b). It is further found at $\sigma = 3.5$ that the spiral shape of the TLV is gradually distorted with decreasing intensity along the mainstream, and eventually being breakdown downstream.

At the heavy cavitation stage $\sigma = 2.2$, the TLV develops in a completely different pattern to that at $\sigma = 3.5$. Firstly, the duct shear vortex is rarely observed on the duct outer surface and downstream. The profile of duct is designed as an airfoil shape in current study, the cavitation occurs at the LE of duct at $\sigma = 2.2$. The formation of cavitation causes flow separation on the outer surface of duct and therefore leads to the weakening of the duct shear vortex. It should be noted that the focus of this study is mainly on the rotor cavitation, thus ignoring the potential cavitation on stator blades and duct. Moreover, the short-wave instability of TLV still presents at $\sigma = 2.2$. The TLV looks stronger with a more delayed breakdown downstream. The instability inception point of TLV is marked by the black dashed line according to the definition proposed by Felli et al. (2011). The instability of TLV is triggered earlier at $\sigma = 2.2$ accompanied with significant mutual interference between adjacent tip vortex filaments.

Comparing the TLV structures under the two cavitation conditions, it is found that the degree of instability for the TLV outflowing the duct is similar, indicating that the cavitation around the rotor tip region has a small effect on the TLV instability in the wake field. As discussed in section 4.2.1, the shape of TLV is somewhat distorted in the incipient stage at the heavy cavitation condition, however this is rapidly corrected as the TLV moves towards the duct outlet under the restraint of shrink duct. The strength of the TLV is slightly enhanced in the wake field at $\sigma = 2.2$, which is the result of the cavitation-vortex interaction at the incipient region. The starting of instability for TLV at $\sigma = 2.2$ is earlier than at $\sigma = 3.5$, while its dissipation downstream is more delayed. The thrust loading of rotor drops significantly at heavy cavitation condition $\sigma = 2.2$, which in turn leads to the decrease of axial ejection velocity in the core region of the PJP wake field. The reduction in axial velocity would further cause the smaller spiral-to-spiral distance between the adjacent TLVs, and consequently increase the mutual interference between consecutive spirals of the TLVs. This is one of the potential reasons for the earlier TLV instability triggering at $\sigma = 2.2$. Another possible reason is the interaction between the TLV and sheet cavity induced shedding vortices, which will be described in the next section. For the different levels of TLV dissipation at different cavitation conditions, it is speculated that this is mainly due to the different axial velocities in the core region of the wake field. The large axial flow velocity accelerates the transport of the TLV downstream, which in turn facilitates its viscous dissipation.

and colored by velocity. (a) $\sigma = 3.5$, (b) $\sigma = 2.2$.

4.4. Effects of cavitation on trailing edge vortices interaction

As with TLV cavitation, the sheet cavitation occurs on the rotor blade surface as the ambient pressure decreases. It is observed from the surface streamlines shown in Fig. 16 that the intense flow separation happens around the TE of blade SS at heavy cavitation condition $\sigma = 2.2$. The backflow at the blade TE gathers with the main flow and flows radially towards the blade tip, this is known as the radial re-entrant flow (David Y. Tan et al., 2012b). The radial re-entrant flow is hardly able to induce

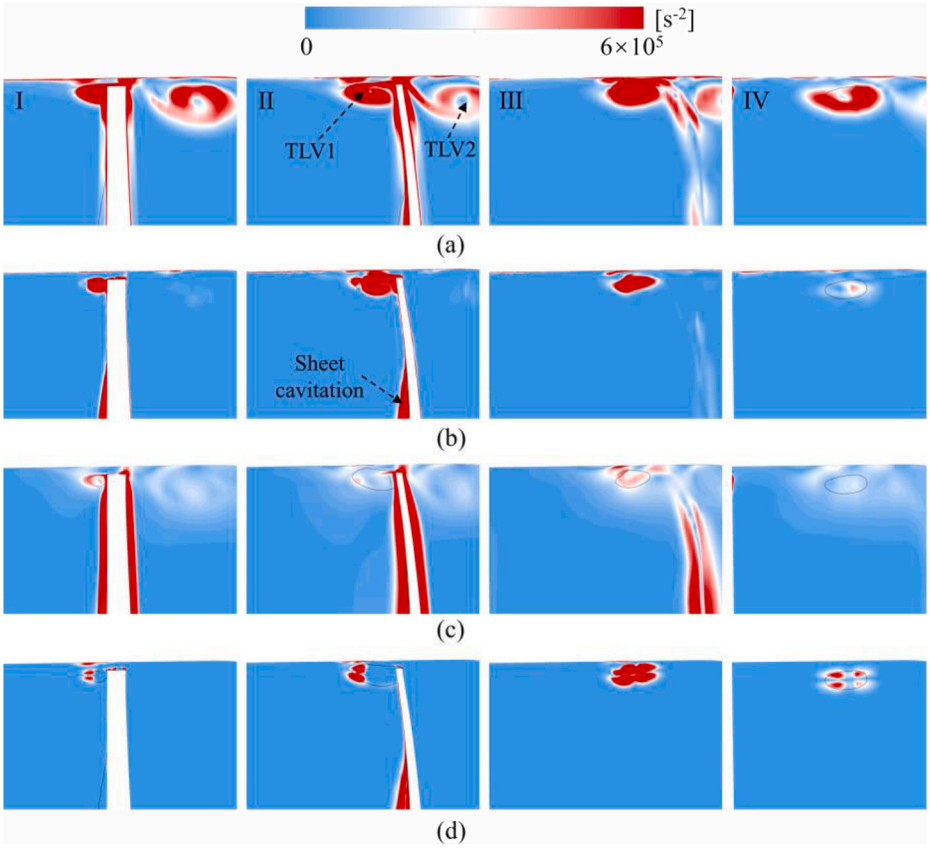

Fig. 19. The different terms of vorticity transport equation on different slices at $\sigma = 2.2$. (a) stretching term, (b) dilatation term, (c) Coriolis force term, (d) baroclinic torque term.

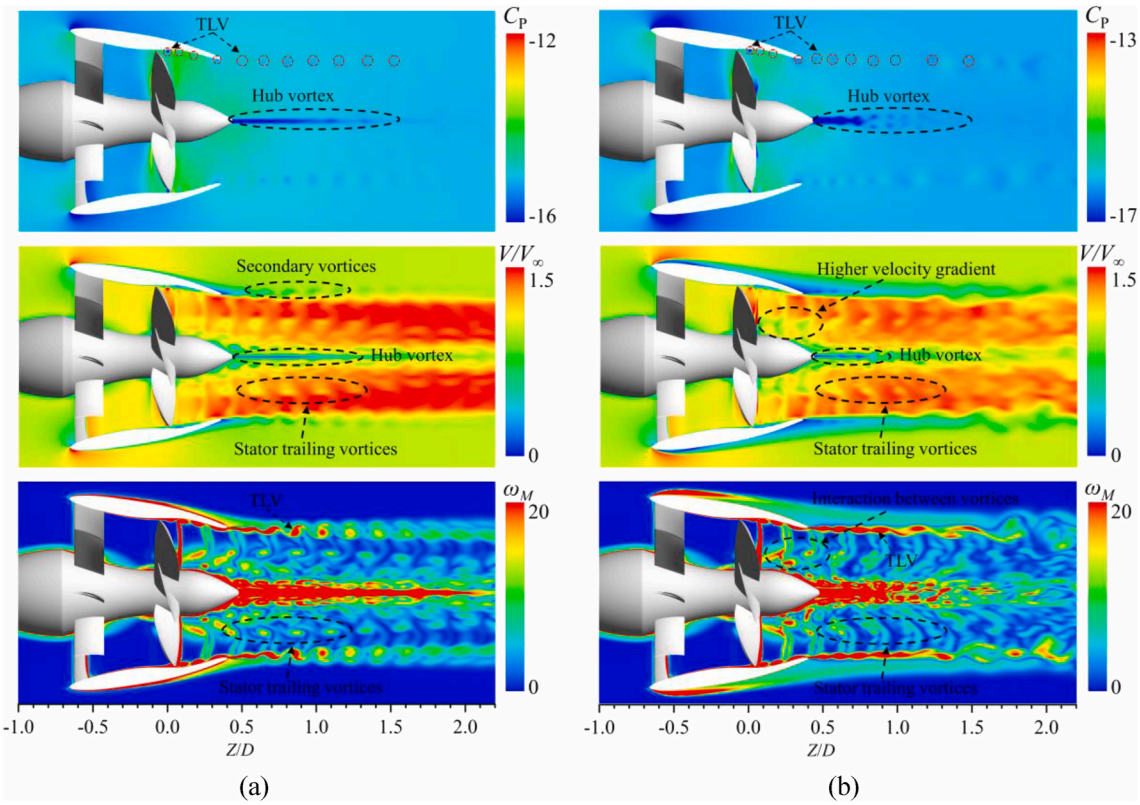

Fig. 20. Distributions of pressure, velocity, and vorticity in the wake field. (a) $\sigma = 3.5$, (b) $\sigma = 2.2$.

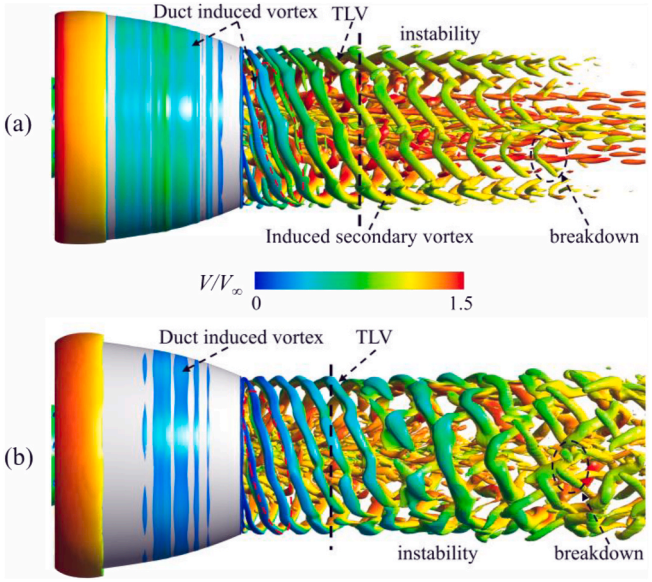

Fig. 21. The TLV structures in the wake field identified by the *Q*-criterion ($Q = 5000s^{-2}$).

the shedding of sheet cavity to large-scale cavities on the rotating blade with slender shape and low attack angle (Zhao et al., 2021b). However, its induced flow separation could increase the trailing vortex shedding. Analysis of the velocity and vorticity fields in Fig. 20 reveals that there is a stronger interaction between vortices behind the rotor at $\sigma = 2.2$, which has a higher velocity gradient. Fig. 22 shows the half view of the wake vortex system at different cavitation stages. It can be clearly seen that a strong trailing vortex sheds off from the blade root of stator and interferes with the rotating rotor. This stator root vortex is cut off by the rotor blade, forming many small-scale vortices downstream of the rotor. It is readily apparent that there are more small-scale vortices downstream of the rotor under heavy cavitation condition, as marked by the black dashed ellipse. To further investigate the interaction process between the stator trailing vortices and the rotating rotor as well as the sheet cavitation induced shedding vortices, the spatial-temporal evolution of the PJP trailing vortex system is extracted under different cavitation conditions.

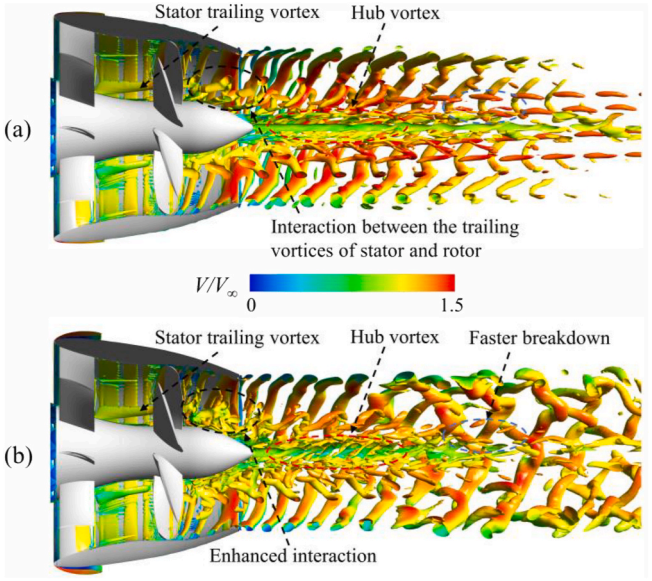

Fig. 22. The TLV structures in the wake field identified by the *Q*-criterion ($Q = 5000s^{-2}$) and colored by velocity. (a) $\sigma = 3.5$, (b) $\sigma = 2.2$.

Figs. 23 and 24 show the complete interaction process between the stator trailing vortices and the rotor within 0.4T, respectively, where T represents a rotating cycle of rotor. At light cavitation stage $\sigma = 3.5$, as marked by the black dashed ellipses in Fig. 23, a strong stator trailing vortex is touching on the blade SS near the TE at t_0+1/22.5T. With the rotor rotating, this trailing vortex is cutting off by the following rotor blade at t_0+3/22.5T, and the short segment vortex is forming at the blade PS accordingly. At t_0+4/22.5T, the downstream end of the short segment vortex is merging with the rotor root trailing vortex, the U-shaped vortex is subsequently restructuring during the t_0+4/22.5T to t_0+8/22.5T. At t_0+9/22.5T, the U-shaped vortex is preparing to break up into two vortex segments and eventually dissipates downstream under viscous effect. Similar to this interaction process, each stator trailing vortex interferes with the rotor blades one after the other, forming many vortex filaments with different scales downstream of the rotor. At the heavy cavitation stage $\sigma = 2.2$, due to the thicker sheet cavities on rotor blade SS, the stator trailing vortex directly interacts with the sheet cavity induced vortices before being cut off by the rotor. During the t_0+3/22.5T to t_0+7/22.5T, the severed stator trailing vortex quickly merges with the cavity induced vortices. Due to the continuous disturbance of some small-scale shedding vortex filaments, the merged U-shaped vortex starts to breakdown at t_0+8/22.5T, resulting in more broken vortex filaments. The trailing vortices are dissipated more quickly after experiencing enhanced interaction in heavy cavitation condition, as evident from vorticity field in Fig. 20 and also Figs. 22–24. Moreover, it is found in Figs. 20 and 22 that the hub vortex presents a more stable shape in the downstream at $\sigma = 3.5$, while it transits faster into the unstable pattern and finally breakdown at $\sigma = 2.2$ when the massive small vortices around the rotor hub flow downstream and interacts with the hub vortex. It could be concluded that the stator trailing vortex inevitably interacts with the sheet cavities at the blade SS, which increases the instability of the attached cavities and vortex shedding. On the other hand, the trailing vortices induced by sheet cavities shed and interact with the severed stator trailing vortices in the rotor outlet, undergoing an evolution process of colliding, merging, and disintegrating, which deteriorates the stability of the trailing vortex system downstream of the PJP. The sheet cavities and trailing vortices interact with each other, which could increase the hydraulic excitation of the PJP.

Fig. 25 presents the vorticity contours on a series of transverse planes downstream of the rotor. At 0.1D, the stator trailing vortices shedding from eight stator blades are obvious and some of them merged with the rotor trailing vortices. It is obvious that the trailing vortices of rotor are stronger at $\sigma = 2.2$ due to more cavity induced shedding vortices. Whereafter, the rotor trailing vortices undergo the roll-up process due to its velocity gradient in the radius direction (Qin et al., 2022), the stator trailing vortices totally interacts with the rotor trailing vortices at 0.3D, there are more small-scale vortex filaments generated at heavy cavitation stage $\sigma = 2.2$. Moreover, it is clearly observed at 0.3D-0.9D that the upper part of rotor trailing vortices gradually touches on the TLVs, so that a dynamic interaction between the rotor trailing vortex and the TLV occurs, which is also observed in Fig. 20. This interaction is enhanced by the cavitation induced vortices at $\sigma = 2.2$, which is another potential reason to earlier trigger the instability of TLV under heavy cavitation condition.

5. Conclusions

In this paper, numerical simulations of cavitating flow in a pre-swirl stator PJP are carried out based on the DDES method coupled with a homogeneous cavitation model. The cavitation patterns and hydrodynamic loadings of the rotor, the cavitation effects on the evolution of TLV in near and far field, and the interaction between trailing vortices of PJP are contrastively analyzed under two typical cavitation conditions. The conclusions are summarized as follows:

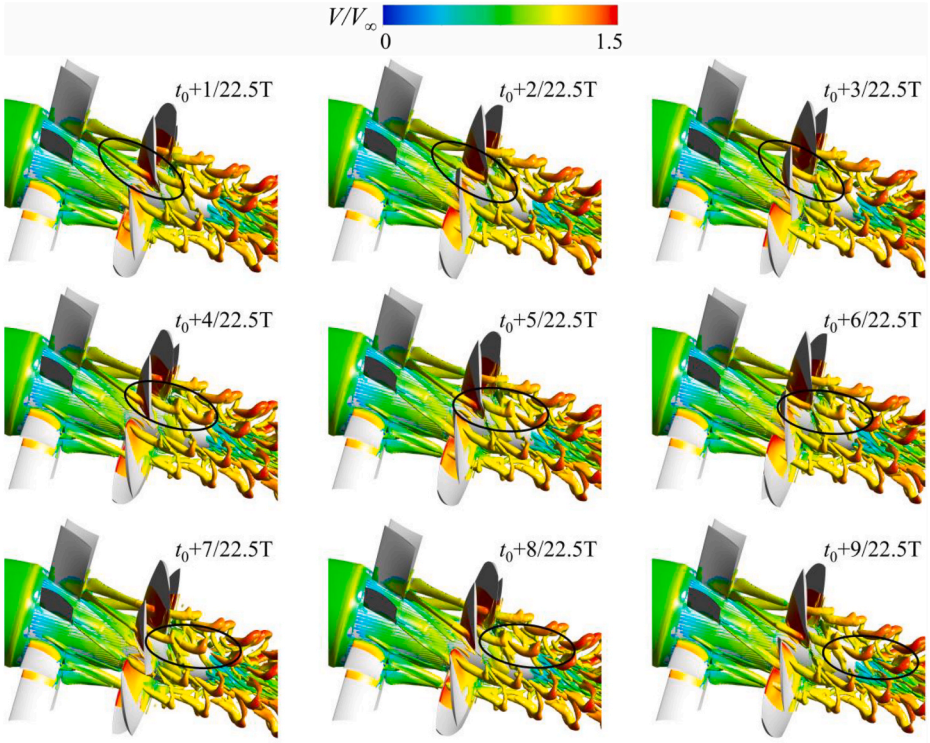

Fig. 23. The spatial-temporal evolution of the trailing vortex system of PJP at $\sigma = 3.5$.

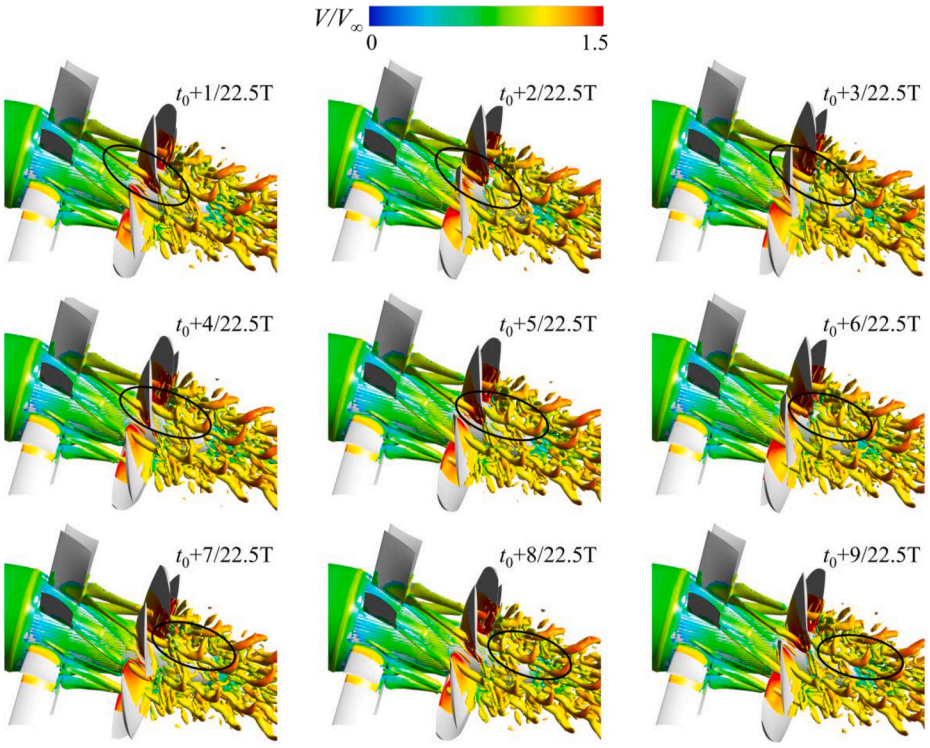

Fig. 24. The spatial-temporal evolution of the trailing vortex system of PJP at $\sigma = 2.2$.

(1) The tip clearance cavitation, TLV cavitation and blade sheet cavitation are considered as the main cavitation types for the rotor of pre-swirl stator PJP. The blade sheet cavities are disturbed by the unsteady wake flow of pre-swirl stator, which distribute non-uniformly on adjacent rotor blades under the effect of phase difference between each single blade of stator and rotor. The interaction between the proliferating blade sheet cavity with the pre-swirl stator wake causes the dominant frequencies of rotor loading to shift from the rotor blade passing

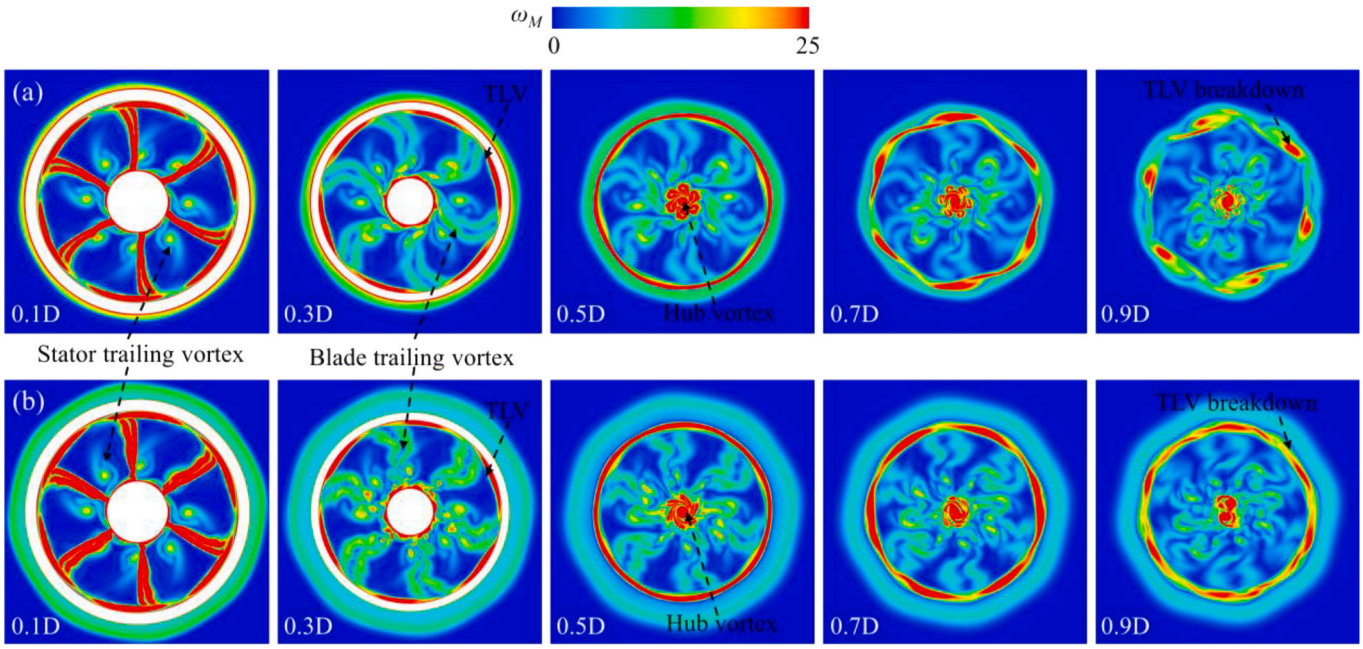

Fig. 25. Distributions of vorticity on different transverse planes at different cavitation conditions. (a) $\sigma = 3.5$, (b) $\sigma = 2.2$.

frequency f_{BPF} and its harmonics to stator blade passing frequency f_s and its harmonics.

(2) The effect of cavitation on TLV evolution is analyzed in both near and far field. Analysis of relative vorticity transport equation reveals that the stretching term dominates the transport of TLV vorticity in the incipient stage. The dilatation and baroclinic torque terms also have a strong influence on the evolution of the TLV especially when cavitation is severe. Cavitation around the tip region promotes the vorticity increment and further strengthens the TLV downstream. In the far field, the TLV presents increased intensity and stronger instability under the heavy cavitation stage. The enhanced mutual interference between consecutive spirals of the TLVs due to the decrease of rotor thrust loading and the increased interaction between the TLV and sheet cavity induced shedding vortices are the main mechanism for the earlier triggering of TLV instability at heavy cavitation condition.

(3) Cavitation affects the evolution of trailing vortex system in pre-swirl stator PJP. The stator trailing vortices interact with the blade sheet cavity, which increases the instability of the sheet cavity and vortex shedding. On the other hand, the induced shedding vortices interact with the severed stator trailing vortices behind the rotor, undergoing an evolution process of colliding, merging, and disintegrating, which deteriorates the stability of the trailing vortex system. The sheet cavities and trailing vortices interact with each other, which could increase the hydraulic excitation of the PJP.

CRediT authorship contribution statement

Xutao Zhao: Conceptualization, Methodology, Software, Formal analysis, Writing – original draft, Writing – review & editing. **Xi Shen:** Methodology, Software, Writing – review & editing. **Linlin Geng:** Writing – review & editing. **Desheng Zhang:** Project administration, Writing – review & editing, Supervision. **B.P.M. (Bart) van Esch:** Writing – review & editing.

Declaration of competing interest

The authors declare that they have no known competing financial interests or personal relationships that could have appeared to influence the work reported in this paper.

Data availability

Data will be made available on request.

Acknowledgments

This work was financially supported by National Natural Science Foundation of China (Grant Nos. 51979125), Jiangsu Provincial Science Fund for Distinguished Young Scholars (Grant No. BK20211547), Technological Innovation Team Project in Colleges and Universities of Jiangsu Province (Grant No. SKJ (2021)-1), Innovation Project for Postgraduates of Jiangsu Province (Grant No. KYCX21_3346).

Nomenclature

Symbols

J	advanced coefficient
V_∞	the uniform oncoming velocity
K_{Tr}	rotor thrust coefficient
λ	blade chord ratio
K_{Qr}	rotor torque coefficient
$K_{Tr,p}$	pressure force coefficient
η_r	rotor efficiency

$K_{Tr,v}$	viscous force coefficient
σ	cavitation number
K'_{Tb}	normalized single blade thrust
K_{Qs}	stator torque coefficient
C_{IPF}	pressure fluctuation intensity coefficient
K_T	total thrust coefficient
C_{P}	pressure coefficient
η_a	PJP efficiency
ω_M	normalized vorticity magnitude

Abbreviations

PJP	pump-jet propulsor
TLV	tip leakage vortex
PS	pressure surface
SS	suction surface
LES	large eddy simulation
DES	detached eddy simulation
DDES	delayed detached eddy simulation
SST	shear stress transport
LE	leading edge
TE	trailing edge
CFD	computational fluid dynamics
FFT	Fast Fourier Transform

References

Celik, I.B., Ghia, U., Roache, P.J., Freitas, C.J., 2008. Procedure for estimation and reporting of uncertainty due to discretization in CFD applications. J. Fluid. Eng. Trans. ASME 130 (7).

Chen, H., Doeller, N., Li, Y., Katz, J., 2020. Experimental investigations of cavitation performance breakdown in an axial waterjet pump. J. Fluid Eng. 142 (9).

Chen, J., Huang, B., Liu, T., Wang, Y., Wang, G., 2021. Numerical investigation of cavitation-vortex interaction with special emphasis on the multistage shedding process. Appl. Math. Model. 96, 111–130.

Cheng, H.Y., Bai, X.R., Long, X.P., Ji, B., Peng, X.X., Farhat, M., 2020. Large eddy simulation of the tip-leakage cavitating flow with an insight on how cavitation influences vorticity and turbulence. Appl. Math. Model. 77, 788–809.

Fei, Z., Zhang, R., Xu, H., Feng, J., Mu, T., Chen, Y., 2022. Energy performance and flow characteristics of a slanted axial-flow pump under cavitation conditions. Phys. Fluids 34 (3).

Felli, M., Camussi, R., Di Felice, F., 2011. Mechanisms of evolution of the propeller wake in the transition and far fields. J. Fluid Mech. 682, 5–53.

Ge, M., Svennberg, U., Bensow, R.E., 2020. Investigation on RANS prediction of propeller induced pressure pulses and sheet-tip cavitation interactions in behind hull condition. Ocean. Eng. 209.

Gong, J., Guo, C.-y., Zhao, D.-g., Wu, T.-c., Song, K.-w., 2018. A comparative DES study of wake vortex evolution for ducted and non-ducted propellers. Ocean. Eng. 160, 78–93.

Gong, J., Ding, J., Wang, L., 2021. Propeller–duct interaction on the wake dynamics of a ducted propeller. Phys. Fluids 33 (7).

Gopalan, S., Katz, J., 2000. Flow structure and modeling issues in the closure region of attached cavitation. Phys. Fluids 12 (4), 895–911.

Han, C.-z., Xu, S., Cheng, H.-y., Ji, B., Zhang, Z.-y., 2020. LES method of the tip clearance vortex cavitation in a propelling pump with special emphasis on the cavitation-vortex interaction. J. Hydrodyn. 32 (6), 1212–1216.

Huang, B., Ducoin, A., Young, Y.L., 2013. Physical and numerical investigation of cavitating flows around a pitching hydrofoil. Phys. Fluids 25 (10).

Huang, B., Zhao, Y., Wang, G., 2014. Large Eddy Simulation of turbulent vortex-cavitation interactions in transient sheet/cloud cavitating flows. Comput. Fluids 92, 113–124.

Huang, R.F., Ji, B., Luo, X.W., Zhai, Z.H., Zhou, J.J., 2015. Numerical investigation of cavitation-vortex interaction in a mixed-flow waterjet pump. J. Mech. Sci. Technol. 29 (9), 3707–3716.

Huang, R., Wang, Y., Du, T., Luo, X., Zhang, W., Dai, Y., 2021. Mechanism analyses of the unsteady vortical cavitation behaviors for a waterjet pump in a non-uniform inflow. Ocean. Eng. 233.

Ji, B., Luo, X., Peng, X., Wu, Y., Xu, H., 2012a. Numerical analysis of cavitation evolution and excited pressure fluctuation around a propeller in non-uniform wake. Int. J. Multiphas. Flow 43, 13–21.

Ji, B., Luo, X., Wu, Y., Peng, X., Xu, H., 2012b. Partially-Averaged Navier–Stokes method with modified k–ε model for cavitating flow around a marine propeller in a non-uniform wake. Int. J. Heat Mass Tran. 55 (23–24), 6582–6588.

Ji, B., Luo, X.W., Arndt, R.E.A., Wu, Y.L., 2014. Numerical simulation of three dimensional cavitation shedding dynamics with special emphasis on cavitation-vortex interaction. Ocean. Eng. 87, 64–77.

Ji, X.-Q., Dong, X.-Q., Yang, C.-J., 2021. Attenuation of the tip-clearance flow in a pump-jet propulsor by thickening and raking the tips of rotor blades: a numerical study. Appl. Ocean Res. 113.

Jiao, W.X., Chen, H.J., Cheng, L., Zhang, B.W., Yang, Y., Luo, C., 2022. Experimental study on flow evolution and pressure fluctuation characteristics of the underwater suction vortex of water jet propulsion pump unit in shallow water. Ocean. Eng. 266, 112569.

Kumar, P., Mahesh, K., 2017. Large eddy simulation of propeller wake instabilities. J. Fluid Mech. 814, 361–396.

Laborde, R., Chantrel, P., Mory, M., 1997. Tip clearance and tip vortex cavitation in an axial flow pump. J. Fluid. Eng. Trans. ASME 119, 680–685.

Li, H., Huang, Q., Pan, G., Dong, X., 2020. The transient prediction of a pre-swirl stator pump-jet propulsor and a comparative study of hybrid RANS/LES simulations on the wake vortices. Ocean. Eng. 203.

Li, H., Huang, Q., Pan, G., Dong, X., 2021. Wake instabilities of a pre-swirl stator pump-jet propulsor. Phys. Fluids 33 (8), 085119.

Liu, M., Tan, L., Cao, S., 2019. Cavitation–vortex–turbulence interaction and one-dimensional model prediction of pressure for hydrofoil ALE15 by large eddy simulation. J. Fluid Eng. 141 (2).

McCormick, B.W., ElSenhuth, J.J., 1963. Design and performance of propellers and pumpjets for underwater propulsion. AIAA J. 1 (10), 2348–2354.

Qin, D., Huang, Q., Shi, Y., Pan, G., Shi, Y., Dong, X., 2021a. Comparison of hydrodynamic performance and wake vortices of two typical types of pumpjet propulsor. Ocean. Eng. 224.

Qin, D.H., Huang, Q.G., Pan, G., Shi, Y., Han, P., Dong, X.G., 2021b. Effect of the duct and the pre-swirl stator on the wake dynamics of a pre-swirl pumpjet propulsor. Ocean. Eng. 237.

Qin, D., Huang, Q., Pan, G., Chao, L., Luo, Y., Han, P., 2022. Effect of the odd and even number of blades on the hydrodynamic performance of a pre-swirl pumpjet propulsor. Phys. Fluids 34 (3).

Rains, D.A., 1954. Tip Clearance Flows in Axial Flow Compressors and Pumps. California Institute of Technology, California, USA.

Shen, X., Zhang, D.S., Xu, B., Shi, W.D., van Esch, B.P.M., 2021. Experimental and numerical investigation on the effect of tip leakage vortex induced cavitating flow on pressure fluctuation in an axial flow pump. Renew. Energy 163, 1195–1209.

Shirazi, A.T., Nazari, M.R., Manshadi, M.D., 2019. Numerical and experimental investigation of the fluid flow on a full-scale pump jet thruster. Ocean. Eng. 182, 527–539.

Spalart, P.R., Deck, S., Shur, M.L., Squires, K.D., Strelets, M.K., Travin, A., 2006. A new version of detached-eddy simulation, resistant to ambiguous grid densities. Theor. Comput. Fluid Dynam. 20 (3), 181–195.

Sun, T.Z., Xie, Q.M., Li, X.M., Zou, L., 2021. Numerical investigation of the effects of free surface on tip-leakage vortex cavitation behaviors over a NACA0009 hydrofoil. Int. J. Multiphas. Flow 141.

Sun, S., Zhi, Y., Li, X., Guo, Z., 2022. Numerical investigation on cavitating wake dynamic of a propeller with bionic tubercle leading-edge. Ocean. Eng. 252.

Suryanarayana, C., Satyanarayana, B., Ramji, K., 2010a. Performance evaluation of an underwater body and pumpjet by model testing in cavitation tunnel. Int. J. Nav. Archit. Ocean Eng. 2 (2), 57–67.

Suryanarayana, C., Satyanarayana, B., Ramji, K., Nageswara Rao, M., 2010b. Cavitation studies on axi-symmetric underwater body with pumpjet propulsor in cavitation tunnel. Int. J. Nav. Archit. Ocean Eng. 2 (4), 185–194.

Tan, L., Sun, W., 2020. Cavitation-vortex-pressure fluctuation interaction in a centrifugal pump using bubble rotation modified cavitation model under partial load. J. Fluid Eng. 142 (5).
Tan, David Y., Miorini, R.L., Keller, Jens, Katz, J., 2012a. Flow Visualization Using Cavitation within Blade Passage of an Axial Waterjet Pump Rotor. ASME Fluids Engineering Division Summer Meeting USA, pp. 395–404.
Tan, D.Y., Miorini, R.L., Keller, J., Katz, J., Asme, 2012b. Flow Visualization Using Cavitation within Blade Passage of an Axial Waterjet Pump Rotor, ASME Fluids Engineering Division Summer Meeting (FEDSM). PR, Rio Grande, pp. 395–404.
Tan, D., Li, Y.C., Wilkes, I., Vagnoni, E., Miorini, R.L., Katz, J., 2015. Experimental investigation of the role of large scale cavitating vortical structures in performance breakdown of an axial waterjet pump. J. Fluid. Eng. Trans. ASME 137 (11).
Wang, G.Y., Senocak, I., Shyy, W., Ikohagi, T., Cao, S.L., 2001. Dynamics of attached turbulent cavitating flows. Prog. Aero. Sci. 37 (6), 551–581.
Wang, L., Wu, T., Gong, J., Yang, Y., 2021a. Numerical analysis of the wake dynamics of a propeller. Phys. Fluids 33 (9).
Wang, L., Wu, T., Gong, J., Yang, Y., 2021b. Numerical simulation of the wake instabilities of a propeller. Phys. Fluids 33 (12).
Widnall, S.E., 1972. The stability of a helical vortex filament. J. Fluid Mech. 54, 641–663.
Yilmaz, N., Aktas, B., Atlar, M., Fitzsimmons, P.A., Felli, M., 2020. An experimental and numerical investigation of propeller-rudder-hull interaction in the presence of tip vortex cavitation (TVC). Ocean. Eng. 216.
Zhang, D.S., Shi, L., Shi, W.D., Zhao, R.J., Wang, H.Y., van Esch, B.P.M., 2015a. Numerical analysis of unsteady tip leakage vortex cavitation cloud and unstable suction-side-perpendicular cavitating vortices in an axial flow pump. Int. J. Multiphas. Flow 77, 244–259.
Zhang, D.S., Shi, W.D., Pan, D.Z., Dubuisson, M., 2015b. Numerical and experimental investigation of tip leakage vortex cavitation patterns and mechanisms in an axial flow pump. J. Fluid. Eng. Trans. ASME 137 (12).
Zhao, G.S., Cao, L.L., Wu, R., Liang, N., Wu, D.Z., 2021a. Wavelet-based multiresolution analysis of cavitation-induced loading instabilities under phase effect in a waterjet pump. Ocean. Eng. 240.
Zhao, G.S., Liang, N., Zhang, Y., Cao, L.L., Wu, D.Z., 2021b. Dynamic behaviors of blade cavitation in a water jet pump with inlet guide vanes: effects of inflow non-uniformity and unsteadiness. Appl. Ocean Res. 117.
Zwart, Philip J., Gerber, Andrew G., Belamri, T., 2004. A Two-phase Flow Model for Predicting Cavitation Dynamics. International Conference on Multiphase Flow, Yokohama, Japan.